

Recent Progress in Chemical Vapor Deposition of 2D Magnetic Materials

Shuyang Yuan, Yanchang Zhou, Lei Yin,* Xintian Wang, Sheng Jiang, Ziyi Song, Yao Wen, Ruiqing Cheng,* and Jun He*

Magnetic 2D materials have gotten significant attention due to their unique low-dimensional magnetism and potential applications in advanced spintronics, providing a perfect platform for investigating magnetic properties at the 2D limit. The chemical vapor deposition (CVD), known for its simplicity and strong controllability, has become a key technique for fabricating ultrathin magnetic nanosheets. This article systematically reviews recent advancements in CVD-grown magnetic 2D materials, focusing on the effects of growth parameters on material morphologies and properties, and analyzing the construction of heterostructures and their role in magnetic regulation. In addition, various magnetic characterization methods are introduced, and potential applications of these materials in spintronic devices are discussed. By summarizing current challenges, the article provides insights into future research directions, emphasizing the need to improve material stability, Curie temperature, and scalable synthesis to enable practical applications of 2D magnetic materials.

1. Introduction

Since the successful preparation of single layer graphene in 2004,^[1] 2D materials have attracted extensive attentions due to their diverse and remarkable properties, as well as their broad application prospects in electronic,^[2] optoelectronic,^[3] spintronic devices,^[4,5] and catalysis.^[6] Up to now, many kinds of 2D materials have been discovered such as graphene, hexagonal boron

nitride (h-BN),^[7,8] transition metal dichalcogenides (TMDs),^[9–11] oxides^[12–14] and so on. Among the diverse range of 2D materials, some exhibit remarkable low-dimensional magnetic properties, attracting researchers to delve deeply into these fascinating phenomena.

In fact, research on 2D magnetism began many years ago. As early as 1944, Onsager proposed a theory that suggested the possibility of long-range magnetic order in 2D systems. However, in 1966, the introduction of the Mermin-Wagner theorem contradicted Onsager's theory by asserting that long-range magnetic order cannot exist in 2D isotropic Heisenberg systems due to thermal fluctuations. This discovery created significant debates and led to slow progress in the field over the next half-century. Fortunately, the first observation of exchange splitting

in monolayer Co in 1982 indicated the existence of 2D magnetism, keeping a glimmer of hope alive.^[15,16] Until the discovery of van der Waals materials, FePS₃, in 2016, it reignited interest and spurred rapid growth in 2D magnetism research. FePS₃, an antiferromagnetic van der Waals material, demonstrated an Ising-type antiferromagnetic ordering down to the monolayer limit, greatly boosting researchers' confidence and shedding new light on the field.^[17] Shortly thereafter, the most significant breakthrough came in 2017, that is, intrinsic long-range ferromagnetic order was observed in 2D CrI₃ and Cr₂Ge₂Te₆,^[18,19] surpassing the depolarization field and thermal fluctuations predicted by the Mermin-Wagner theorem,^[20–22] thus experimentally confirming the existence of 2D magnetic materials. This plays a crucial role in the fundamental research of low-dimensional spin behavior and propels new spintronic applications, significantly stimulating research enthusiasm in the field of 2D magnetism.

Encouragingly, many novel 2D magnetic materials have been successfully fabricated,^[22–27] providing an ideal platform for exploring magnetism at the 2D limit. They are generally divided into the following seven categories: transition metal halides,^[19,28–37] transition metal oxyhalides,^[38,39] transition metal chalcogenides,^[40–56] transition metal phosphorus sulfides,^[57–62] transition metal oxides,^[63–67] transition metal germanium tellurides,^[18,68–78] transition metal bismuth tellurides.^[79,80] We have compiled typical representatives of each category in Table 1, including magnetic ordering, transition temperature and synthesis technique of these materials. 2D magnetic materials

S. Yuan, Y. Zhou, L. Yin, X. Wang, S. Jiang, Z. Song, Y. Wen, R. Cheng, J. He
 Key Laboratory of Artificial Micro- and Nano-structures of Ministry of Education
 School of Physics and Technology
 Wuhan University
 Wuhan 430072, China
 E-mail: yin-lei@whu.edu.cn; chengrq@whu.edu.cn; He-jun@whu.edu.cn

R. Cheng, J. He
 Hubei LuoJia Laboratory
 Wuhan 430072, China

 The ORCID identification number(s) for the author(s) of this article can be found under <https://doi.org/10.1002/apxr.202400169>

© 2025 The Author(s). Advanced Physics Research published by Wiley-VCH GmbH. This is an open access article under the terms of the Creative Commons Attribution License, which permits use, distribution and reproduction in any medium, provided the original work is properly cited.

DOI: [10.1002/apxr.202400169](https://doi.org/10.1002/apxr.202400169)

Table 1. Summary of 2D magnetic materials.

Classification	Material	Magnetic ordering	Transition temperature	Synthesis technique	Refs.
Transition metal halides	CrI_3	FM	$T_c = 45\text{ K}$ (monolayer) $T_c = 61\text{ K}$ (bulk)	CVT/Exfoliation	[19,28–34]
	CrCl_3	FM/AFM (interlayer)	$T_c = 17\text{ K}$ (few layer)	CVT/Exfoliation	[29,34–36]
	CrBr_3	FM	$T_c = 47\text{ K}$ (bulk)	CVT	[29,36,37]
Transition metal oxyhalides	FeOCl	AFM	$T_N = 83\text{ K}$ (few layer)	CVT	[38]
	VOCl	AFM	$T_N = 82\text{ K}$ (monolayer)	CVT/Exfoliation	[39]
Transition metal chalcogenides	$\alpha\text{-MnSe}$	AFM	$T_N = 160\text{ K}$ (monolayer)	CVD	[40–42]
	$\beta\text{-MnSe}$	FM	$T_c = 42.3\text{ K}$ (few layer)	CVD	[43]
	1T-MnSe_2	FM	$T_c \approx 300\text{ K}$	MBE	[44,45]
	T-FeTe	AFM	$T_N = 70\text{ K}$	CVD	[46–48]
	H-FeTe	FM	$T_c = 220\text{ K}$ (20.2 nm)	CVD	[46–48]
	Fe_5Se_8	FM	$T_c \approx 300\text{ K}$	CVD	[49]
	1T-CrTe_2	FM	$T_c \approx 305\text{--}320\text{ K}$	Flux Method/Exfoliation	[50]
	CrTe	FM	$T_c = 350\text{ K}$ (few layer)	CVD/Exfoliation	[51]
	VSe_2	FM	$T_c \approx 300\text{ K}$ (monolayer)	MBE/Exfoliation	[52,53]
Transition metal phosphorus sulfides	Cr_2S_3	FM	$T_c = 120\text{ K}$ (monolayer)	CVD	[54–56]
	NiPS_3	AFM	$T_N = 155\text{ K}$ (few layer)	CVT	[57–60]
	FePS_3	AFM	$T_N = 118\text{ K}$ (few layer)	Liquid exfoliation	[57,61]
	CrPS_4	AFM	$T_N = 34\text{ K}$ (monolayer)	CVT	[57,62]
Transition metal oxides	MnPS_3	AFM	$T_N = 78\text{ K}$ (monolayer)	CVT	[57]
	$\epsilon\text{-Fe}_2\text{O}_3$	FM	$T_c = 291\text{ K}$ (≈12 nm)	CVD	[63]
	$\gamma\text{-Fe}_2\text{O}_3$	FM	$T_c = 950\text{ K}$	CVD	[64,65]
	CoFe_2O_4	FM	$T_c > 390\text{ K}$ (≈2–4 nm)	CVD	[66]
Transition metal germanium tellurides	Fe_3O_4	FM	$T_c \sim 350\text{ K}$ (1.9 nm)	CVD	[67]
	Fe_3GeTe_2	FM	$T_c = 203\text{ K}$ (few layer)	CVT/Exfoliation	[68–71]
	CrSiTe_3	FM	$T_c = \approx 17\text{--}33\text{ K}$ (≈1.7–7 nm)	Flux Method/Exfoliation	[72–75]
	$\text{Cr}_2\text{Ge}_2\text{Te}_6$	FM	$T_c = 30\text{ K}$ (bilayer) $T_c = 68\text{ K}$ (6L)	CVT/Exfoliation	[18,76–78]
Transition metal bismuth tellurides	MnBi_2Te_4	AFM	$T_c = \approx 20.6\text{--}21.6\text{ K}$ (≈6–7L)	Flux Method/Exfoliation	[79,80]
	$\text{MnBi}_8\text{Te}_{13}$	FM	$T_c = 12\text{ K}$ (7L)		

*FM: Ferromagnetism; AFM: Antiferromagnetism; CVT: Chemical Vapor Transport; CVD: Chemical Vapor Deposition; MBE: Molecular Beam Epitaxy;

typically exhibit novel properties and physical phenomena significantly different from their bulk counterparts and traditional magnetic thin films. For instance, few-layer CrI_3 and $\text{Cr}_2\text{Ge}_2\text{Te}_6$ nanosheets, prepared by mechanical exfoliation, display layer-dependent ferromagnetism at low temperatures.^[18,19] Ultrathin CrTe_2 grown by molecular beam epitaxy (MBE) exhibits ferro-

magnetism even at room temperature.^[24] Notably, Cr_2Te_3 shows an anomalous Curie temperature (T_c) variation with thickness due to structural reconstruction when the thickness decreases. The T_c of 5 nm thick Cr_2Te_3 approaches room temperature (280 K), while for a thickness of 40.3 nm, the T_c decreases to 170 K.^[81] Therefore, fundamental research on spin behavior in 2D

Table 2. The comparison of various 2D magnetic material synthesis technologies.

Synthesis technologies	Advantages	Disadvantages	Refs.
CVD	CVD is one of the most promising techniques for the direct synthesis of large-area 2D materials, which is cost-effective, easy to operate, and suitable for large-scale production. It offers strong controllability, high-quality thin films, and the ability to coat complex shapes.	CVD always requires high temperatures, which may lead to compatibility issues with backend processes. There may also be defects such as grain boundaries and thickness fluctuations that affect device performance. The material growth is highly influenced by the substrate.	[88–92]
CVT/Flux methods	Metastable-phase single crystals can be obtained via CVT, with high crystal quality.	The product is in the form of bulk crystals. Its properties are significantly influenced by stoichiometric ratio and crystal defects. CVT equipment is complex, and the high-temperature reaction leads to higher costs.	[19,29,38,39,50,79,80]
Mechanical exfoliation	Mechanical exfoliation maintains a high crystal structure and crystallinity. The operation and required equipment are simple. By using methods such as noble metal-assisted techniques, large-sized monolayer single crystals can be obtained.	The repeatability and uniformity of the exfoliation method cannot be guaranteed. The yield of thin layers is extremely low. Material selection is limited, and it is only applicable to layered materials.	[52,53,93,94]
Liquid exfoliation	The synthesis conditions of liquid exfoliation are mild, without high temperature. The process is simple, cost-effective, and has a high yield, making it suitable for large-scale production.	Due to the complex chemical environment, defects and foreign materials are likely to be incorporated into the crystals, resulting in poorer crystal quality.	[82,95–97]
MBE	MBE allows for the control of atomic-level growth processes, making it suitable for the fabrication of ultra-high-quality 2D materials and heterostructures.	MBE equipment is expensive, the growth process is complex, and the growth rate is slow, making it unsuitable for large-scale industrial production.	[24,82,87]

magnetic materials is particularly important for advancing new spintronics and spintronic devices,^[82] laying the foundation for the development of multifunctional, high-performance quantum devices.

To date, the majority of available 2D magnetic materials are derived through mechanical exfoliation from high-quality crystalline bulk counterparts.^[83,84] Nonetheless, accurately controlling the thickness and grain size of these samples during fundamental property investigations is challenging, not to mention achieving large-scale, high-yield production for practical applications. Furthermore, certain materials with notable magnetic properties, such as CrI₃, are extremely unstable in atmospheric conditions.^[85] Conducting the entire mechanical exfoliation process within a glovebox is necessary to avoid exposure to oxygen and water, which significantly increases time consumption and operational complexity. Additionally, although MBE is a viable method for producing uniform high-quality magnetic materials,^[86,87] it is neither cost-effective nor time-efficient, limiting its scalability.

Thus, it is essential and urgent to create easy, convenient, and mass-producible synthesis methods for generating magnetic materials. A bottom-up growing method, CVD, has garnered significant interest because of its simple process, low cost, high controllability and scalability.^[88] Regardless of the variations in CVD techniques, the core process remains consistent. First, the transport of reactant gases, also known as precursors, into the reaction chamber. These gases move toward the substrate through the chamber's boundary layer. Upon reaching the substrate, the gases either diffuse through the boundary layer or undergo gas-

phase reactions to form intermediate reactants. The reactants or their intermediates then adsorb onto the heated substrate surface and diffuse across it. At the gas-solid interface, heterogeneous reactions occur, leading to the nucleation, growth, and coalescence of a thin film. Ultimately, by-products generated during the reaction, as well as any unreacted gases, desorb from the substrate and are removed from the reaction zone, ensuring that the final film is clean and free from contaminants.^[88] The CVD process is relatively simple and controllable, establishing its important position across various fields. To better emphasize the advantages of CVD technology, we have prepared **Table 2**, which presents a detailed comparison of the advantages and disadvantages of CVD^[88–92] alongside other 2D material growth techniques, including CVT/Flux methods,^[19,29,38,39,50,79,80] mechanical exfoliation,^[52,53,93,94] liquid exfoliation,^[82,95–97] and MBE.^[24,82,87]

Before entering the field of 2D magnetic materials, CVD technology had already made significant contributions in various areas, including surface modification,^[98–100] 2D materials synthesis,^[101] and flexible electronic devices.^[102] This sequence highlights the versatility of CVD in advancing various fields prior to its adoption in 2D magnetic material research. Nowadays, various 2D materials are prepared by this method, such as graphene,^[103] h-BN,^[104] some TMDs like MoS₂^[105] and some ultrathin nonlayered oxides. Similarly, in recent years, enormous 2D magnetic materials have been successfully prepared via CVD methods with regular morphology and tunable thickness, such as tellurides (TaTe₂,^[106] NbTe₂,^[106] Cr₂Te₃,^[81] Cr₅Te₈,^[107] FeTe^[46]), selenides (CrSe₂,^[108] CrSe,^[109] α -MeSe^[3]), sulfides (Cr₂S₃,^[110] CrS₂^[22]), oxides (CoFe₂O₄,^[66] ϵ -Fe₂O₃^[63]) and single-element

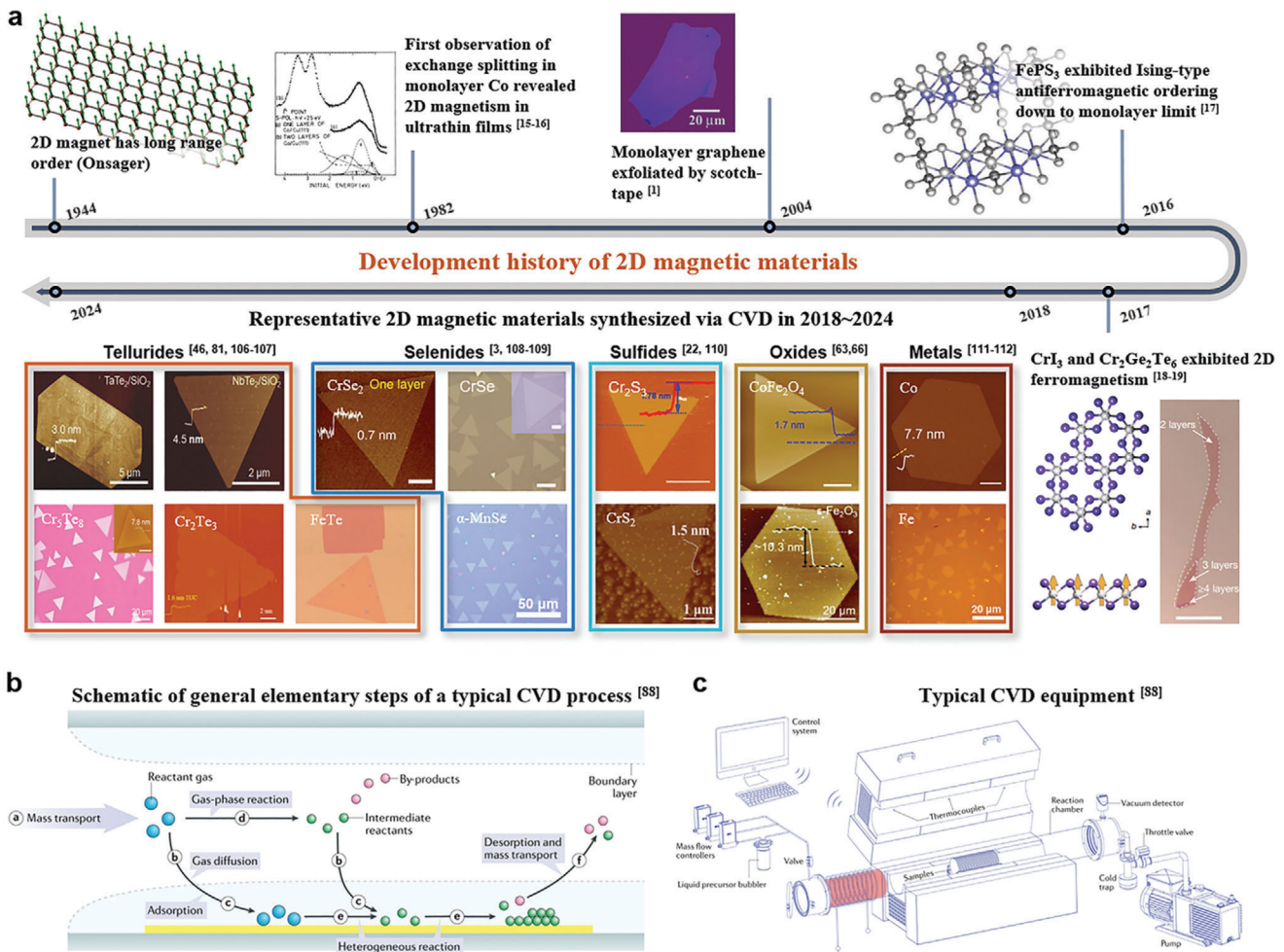


Figure 1. Summary of 2D magnetic materials and brief introduction of CVD. (a) The development history of 2D magnetic materials^[15,16] and various categories of 2D magnetic materials synthesized via CVD in recent years.^[3,22,46,63,66,81,106–112] Reproduced with permission.^[15] Copyright 1982, The American Physical Society. Reproduced with permission.^[1] Copyright 2004, The American Association for the Advancement of Science. Reproduced with permission.^[18] Copyright 2017, Springer Nature. Reproduced with permission.^[19] Copyright 2017, Springer Nature. Reproduced with permission.^[3] Copyright 2021, Wiley-VCH GmbH. Reproduced with permission.^[22] Copyright 2022, Wiley-VCH GmbH. Reproduced with permission.^[46] Copyright 2020, Springer Nature. Reproduced with permission.^[63] Copyright 2023, Wiley-VCH GmbH. Reproduced with permission.^[66] Copyright 2022, Springer Nature. Reproduced with permission.^[81] Copyright 2020, American Chemical Society. Reproduced with permission.^[106] Copyright 2018, Wiley-VCH GmbH. Reproduced with permission.^[107] Copyright 2021, Wiley-VCH GmbH. Reproduced with permission.^[108] Copyright 2021, Springer Nature. Reproduced with permission.^[109] Copyright 2019, Wiley-VCH Verlag GmbH & Co. KGaA, Weinheim. Reproduced with permission.^[110] Copyright 2019, American Chemical Society. Reproduced with permission.^[111] Copyright 2019, Wiley-VCH GmbH. Reproduced with permission.^[112] Copyright 2022, Elsevier. b) Schematic of general elementary steps of a typical CVD process. c) Typical CVD equipment. Reproduced with permission.^[88] Copyright 2021, Springer Nature.

metals (Co,^[111] Fe^[112]). We summarize the above content in Figure 1, showing the milestone events in the development of 2D magnetism, and various 2D magnetic materials prepared by CVD, along with a schematic diagram of typical CVD process and a typical CVD equipment.

In this review, we focus on the key factors influencing the growth and physical properties of 2D magnetic materials via CVD process, such as growth parameters (growth temperature, growth time, and gas flow rate), treatment of precursors and choice of growth substrates on the morphology. We also discuss the application of CVD in magnetic heterostructures preparation. Subsequently, we present the characterization of magnetic proper-

ties and novel magnetic phenomena using various measurement methods. Next, we discuss the application of 2D magnetic materials in electronic devices. Finally, we summarize the existing challenges and provide an outlook on the future of these emerging 2D magnetic materials.

2. Key Factors in CVD Growth

The CVD method, characterized by controllable thickness, fast growth rate, and high yield, holds broad application prospects in achieving the controlled growth of 2D magnetic films.^[88,113] Therefore, in-depth research and summary of the effects of

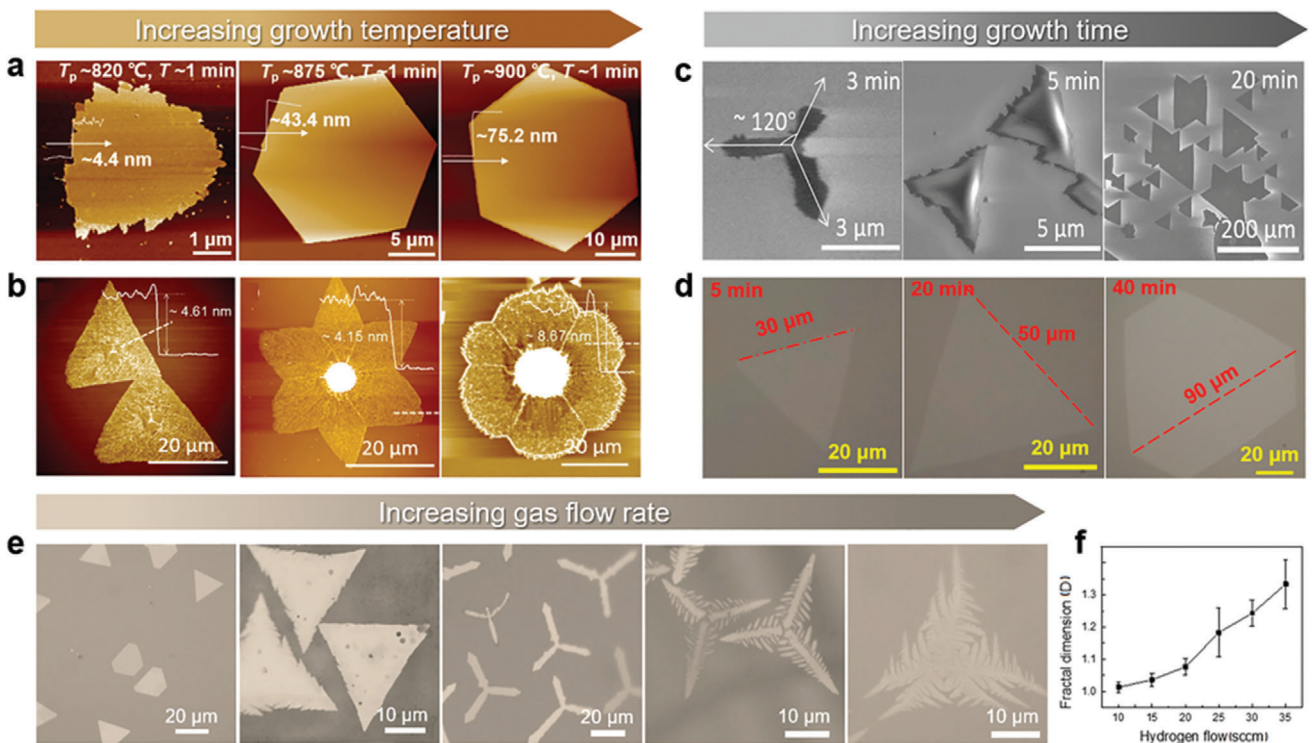


Figure 2. Control of 2D materials' morphology by adjusting growth temperature, time, and gas flow rate. a) AFM images and height profiles of Fe_7S_8 under growth conditions of 1 min at the temperatures of ≈ 820 , ≈ 875 , and $\approx 900^\circ\text{C}$, respectively. Reproduced with permission.^[115] Copyright 2022, American Chemical Society. b) AFM images and height profiles of $\gamma\text{-Fe}_2\text{O}_3$ at different growth temperatures of ≈ 930 , ≈ 980 , and $\approx 1030^\circ\text{C}$ with morphology of triangular, stellated, and petaloid, respectively. c) SEM images of the as-grown $\gamma\text{-Fe}_2\text{O}_3$ nanoflakes with the increase in growth time of ≈ 3 , ≈ 5 , and 20 min, respectively. Reproduced with permission.^[64] Copyright 2021, American Chemical Society. d) OM images of as-grown Cr_2S_3 nanoflakes with the increase in growth time of ≈ 5 , ≈ 20 , and 40 min under the growth temperature of 750°C . Reproduced with permission.^[110] Copyright 2019, American Chemical Society. e) OM images of $\beta\text{-MnSe}$ crystals grown with increasing H₂ flow rates of 15, 20, 25, 30, and 35 sccm, respectively. f) The trend of fractal dimension (D) changes in materials grown under different hydrogen flow rates. Reproduced with permission.^[43] Copyright 2022, The Authors. SmartMat published by Tianjin University and John Wiley & Sons Australia, Ltd.

changes in CVD growth conditions on the regulation of sample morphology, thickness, and performance are beneficial for further improving the CVD growth process and achieving controllable synthesis of high-quality 2D magnetic films. Moreover, the controllable growth through CVD enables the preparation of 2D magnetic heterostructures with smooth surfaces, atomic-sharp interfaces and controllable morphology, promoting the practical application of 2D magnetic materials. In this section, we summarize the regulatory effects of growth conditions on materials and the application of CVD in preparation of magnetic heterostructures.

2.1. Growth Parameters

During the CVD growth process, various factors can significantly impact the performance of the 2D magnetic film.^[114] Among these, the growth parameters are particularly crucial. Growth parameter such as growth temperature, duration, and gas flow rate play a major role in determining the quality, morphology, and functional properties of the resulting samples. During this chapter, we will emphasize the discussion on the regulation effects of growth parameter in the three mentioned cases.

2.1.1. Growth Temperature

Growth temperature is one of the critical parameters influencing the CVD process. Variations in temperature directly affect the decomposition rate of the precursor, the surface reaction kinetics, and the crystal growth rate of the material. An appropriate temperature can enhance the decomposition and migration of reactants, thereby promoting the formation of high-quality crystals. Conversely, insufficient temperature may result in incomplete crystal structures, uneven morphology, even the presence of residual by-products, and excessive temperature may alter the material's morphology, lead to overgrowth, or even trigger unwanted phase transitions.^[26,56,64,107,110,115,116]

As an example, Wang et al. synthesized Fe_7S_8 nanosheets at varying temperatures, showing AFM images along with the corresponding thickness in Figure 2a.^[115] At the synthesis temperature of $\approx 820^\circ\text{C}$, the Fe_7S_8 nanosheets displayed an irregular sheet-like morphology with a thickness of ≈ 4.4 nm. With synthesis temperature raising, the nanosheet assumed a more regular hexagonal shape and a thicker thickness. Further increasing temperature resulted in nanosheets with an even more distinct edge and larger size, with a thickness of ≈ 75.2 nm. The AFM measurements indicate that the thickness of the nanosheets

increases significantly with the synthesis temperature, suggesting that higher temperatures promote faster atomic migration and deposition rates, leading to thicker and larger nanosheets. This temperature-dependent growth behavior highlights the critical role of temperature in determining the thickness and morphology of Fe_7S_8 nanosheets. Excessive thickness may compromise the 2D properties of the material, and irregular morphology can also significantly affect the material's performance. Therefore, it is essential to select an appropriate growth temperature to balance morphology, uniformity and thickness.^[115]

Temperature not only significantly affects material's growth rate, but it also plays a crucial role in determining the growth control mechanisms. For instance, Jia et al. reported that the morphology of 2D magnetic $\gamma\text{-Fe}_2\text{O}_3$ nanosheets is strongly affected by growth temperature during the CVD process.^[64] This is primarily due to a shift in the growth mechanism from thermodynamic to kinetic control as the temperature increases. As illustrated in Figure 2b, at low temperatures, the nanosheets tend to form triangular shapes. This morphology is driven by thermodynamic factors, leading to slower growth and the formation of triangles with relatively smooth edges. When the temperature rises, the nanosheets develop a star-like morphology, characterized by branches extending from the triangular base, resulting in a star-shaped structure. During this phase, the growth remains largely thermodynamically controlled, but as the temperature increases, signs of kinetic control begin to appear. At even higher temperatures ≈ 1030 °C, the nanosheets take on a petal-like morphology, resembling flowers with multiple petals. This shift indicates a pronounced transition to kinetic control, where faster growth rates result in more complex and less symmetrical shapes. In conclusion, Wang and Jia's studies underscore the significant role of growth temperature in controlling the morphology of $\gamma\text{-Fe}_2\text{O}_3$ nanosheets.^[64]

2.1.2. Growth Duration

Jia et al. not only investigated the influence of temperature on the morphology of $\gamma\text{-Fe}_2\text{O}_3$ nanosheets but also further revealed the growth process of these nanosheets.^[64] In their study, the morphology of $\gamma\text{-Fe}_2\text{O}_3$ nanosheets at different growth times was characterized using scanning electron microscopy (SEM). Figure 2c illustrates the morphological evolution of $\gamma\text{-Fe}_2\text{O}_3$ nanosheets at growth times of 3, 5, and 20 min. At the initial growth stage, the nanosheets exhibited a distinct dendritic structure (Figure 2c, left). This indicates that at the initial stage, the crystals grew along specific diffusion paths, resulting in this directionally-oriented dendritic morphology. As the growth time extended, the edges of the dendritic structures began to expand further and gradually developed into clear triangular shapes (Figure 2c, middle). When the growth time was further extended to 20 min, the lateral size of the nanosheets increased significantly, and the originally separated triangular nanosheets connected with each other, forming a large-scale continuous film (Figure 2c, right). This phenomenon indicates that, with longer growth times, the lateral expansion rate of the nanosheets accelerated, ultimately leading to the formation of a large-area film. This finding provides important insights into the mechanism of morphological evolution in nanomaterials and offers new perspec-

tives for controlling material morphology through the regulation of growth time.^[64]

Similarly, researches conducted by Zhang et al. on CrSe^[109] and Chu et al. on Cr₂S₃^[110] also focused on the controlled preparation of these materials. Taking Cr₂S₃ nanosheets as an example, as shown in Figure 2d, during the initial growth stage, the formed Cr₂S₃ crystals were small, exhibiting dispersed small triangular structures with edge lengths of 30 micrometers. As the growth time extended, the crystal size increased significantly, forming triangular structures with edge lengths of ≈ 50 micrometers. When the growth time was further extended to 40 min, the crystal size increased further, forming larger triangular crystals with more regular morphology and smoother edges.^[110]

2.1.3. Gas Flow Rate

Except temperature and duration, gas flow rate is also a critical parameter in the growth of 2D magnetic nanosheets.^[3,40,43,63] Zhang et al. conducted an in-depth study on $\alpha\text{-MnSe}$,^[3] and Zou et al. focused on $\beta\text{-MnSe}$,^[43] examining the regulation of nanosheet samples by gas flow rate. It was observed that the gas flow rate had a significant effect on parameters such as sample thickness and morphology.

Taking Zou et al.'s study as an example,^[43] Figure 2e presents images of $\beta\text{-MnSe}$ crystals grown under different hydrogen flow rates, ranging from 15 to 35 sccm. As the hydrogen flow rate increased, the shapes of these crystals gradually evolved from simple triangles to windmills, dendrites, and finally to snowflake structures. This growth mechanism is attributed to a diffusion-limited process. At lower hydrogen flow rates, Mn and Se atoms have sufficient time to diffuse across the substrate surface, forming regular triangular shapes. However, as the hydrogen flow rate increases, the diffusion rate accelerates, favoring the growth of the Mn-terminated edge, which is more energetically favorable. Figure 2f quantitatively supports this observation by showing the relationship between the fractal dimension of $\beta\text{-MnSe}$ crystals and hydrogen flow rate.^[43] The fractal dimension, which measures the complexity of the crystal shape, increased from ≈ 1.02 to 1.4 as the hydrogen flow rate increased, indicating a direct correlation between flow rate and the complexity of crystal morphology.^[43] Furthermore, Zhang et al.'s study revealed a negative correlation between gas flow rate and sample thickness,^[3] corroborating Zou et al.'s findings. Understanding these growth dynamics is crucial for optimizing the synthesis of 2D magnetic semiconductors and paving the way for their potential applications in spintronic devices.^[3]

2.2. Precursor

In the process of CVD, the precursor is another crucial factor influencing growth. For instance, the distance between the precursor source and the substrate can impact the coverage of the sample,^[26,109] the mass of the precursor affects the elemental ratio in the nanosheets,^[112,117] and the type of precursor can influence the phase structure of the material, ultimately affecting its magnetic performance.

Zhang et al. systematically studied the impact of the distance between the precursor source and the substrate (D_{ss}) on the

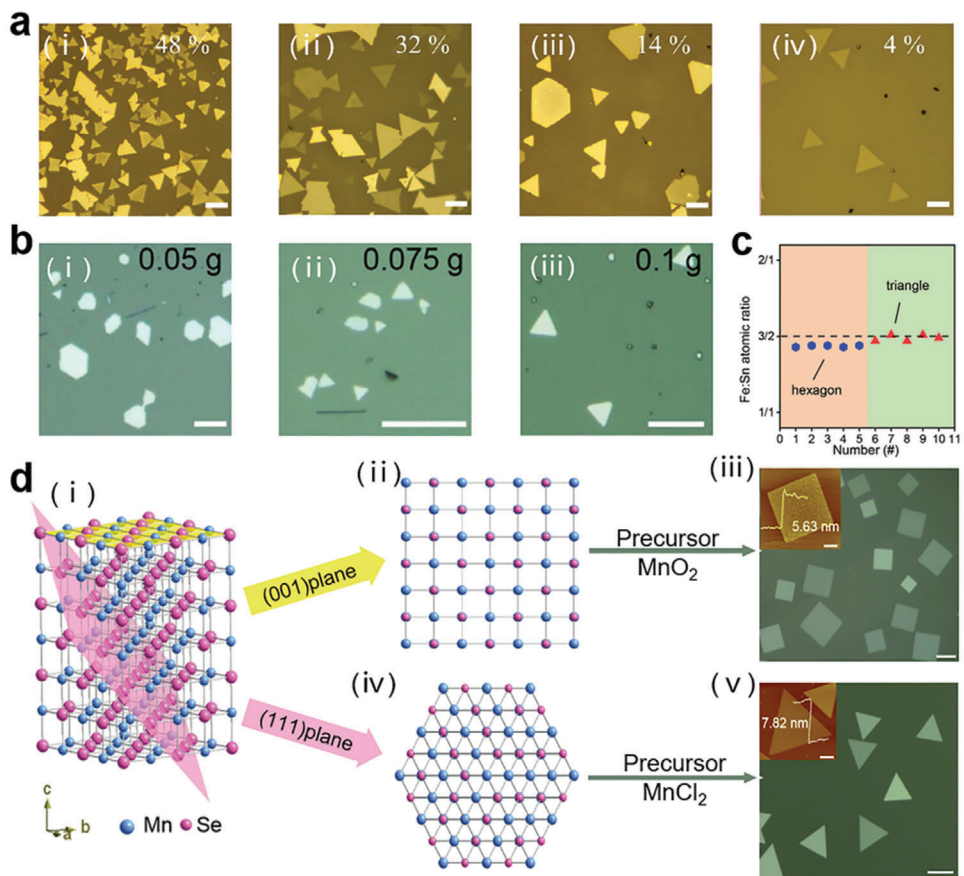


Figure 3. Regulation of 2D magnetic nanosheets through D_{ss} , precursor mass, and precursor type. a) The OM images of as-grown Cr_5Te_8 flakes, synthesized under identical conditions at 800°C . The coverage of the flakes varies depending on the D_{ss} : 48% coverage at a D_{ss} of $\approx 2\text{ cm}$ (i), 32% at 4 cm (ii), 14% at 6 cm (iii), and 4% at 8 cm (iv). Scale bar: $20\text{ }\mu\text{m}$. Reproduced with permission.^[26] Copyright 2023, American Chemical Society. b) OM images of Fe_3Sn_2 nanosheets from precursor FeCl_2 with mass of 0.05 (i), 0.075 (ii) and 0.1 g (iii), respectively. Scale bars: $20\text{ }\mu\text{m}$. c) Statistical Fe:Sn atomic ratios of Fe_3Sn_2 nanosheets with the shapes of hexagons and triangles. Reproduced with permission.^[117] Copyright 2024, American Chemical Society. d) $\alpha\text{-MnSe}$ synthesized by different precursor (i) Diagrams of the crystal structure of $\alpha\text{-MnSe}$, with blue spheres indicating Mn atoms and red spheres representing Se atoms. The yellow shading highlights the (001) lattice plane (ii), while the red shading corresponds to the (111) lattice plane (iv). iii,v) OM image of as-grown square (iii) / triangular (v) $\alpha\text{-MnSe}$ nanosheets. Scale bar: $20\text{ }\mu\text{m}$. The inset is a typical AFM image. Scale bar: $2\text{ }\mu\text{m}$. Reproduced with permission.^[41] Copyright 2021, Royal Society of Chemistry.

coverage of Cr_5Te_8 crystals during CVD synthesis. As shown in Figure 3a, the crystal coverage and nucleation density decrease significantly with increasing D_{ss} . The main reason is that as D_{ss} increases, the precursor concentration decreases, leading to a sparser distribution of Cr_5Te_8 crystals, which ultimately results in fewer but larger crystal regions. There is an inverse relationship between coverage and crystal size. Therefore, optimizing the D_{ss} is essential to find the best balance between ensuring sufficient coverage and obtaining larger crystal sizes.^[26]

Additionally, Zhu et al. investigated the regulation of Fe_3Sn_2 nanosheet morphology and magnetic properties by varying the mass of FeCl_2 precursor.^[117] As shown in Figure 3b, with the increase in FeCl_2 mass, the Fe_3Sn_2 nanosheets gradually transition from a hexagonal to a triangular shape. This morphological evolution is directly related to changes in the Fe/Sn atomic ratio. Lower precursor mass results in an Fe/Sn atomic ratio a bit lower than 3:2, leading to the formation of hexagonal nanosheets. With the precursor mass increases, the Fe/Sn atomic ratio approaches the ideal stoichiometric ratio of 3:2, resulting in the formation of

triangular nanosheets, as illustrated in Figure 3c. These changes in morphology and elemental composition significantly impact the magnetic properties of the material. Hexagonal nanosheets, with more Fe vacancies, exhibit weaker magnetism, whereas triangular nanosheets display stronger ferromagnetism and pronounced magnetic hysteresis.^[117]

The type of precursor also has a significant regulatory effect on magnetic nanosheets. Li et al. achieved precise control over the morphology and growth direction of $\alpha\text{-MnSe}$ 2D nanosheets by introducing different manganese precursor sources.^[41] The result is shown in Figure 3d. When MnO_2 is selected as the manganese precursor, the $\alpha\text{-MnSe}$ nanosheets grow along the (001) crystal plane, forming square nanosheets with a thickness of 5.63 nm, as shown in Figure 3d(i,ii,iii). This growth method is considered to be a stepwise reaction process in which MnO_2 gradually transforms into an $\alpha\text{-MnSe}$ (001) plane structure with a larger lattice parameter during the selenization process. While MnCl_2 is used as the precursor, the sample grow along the (111) crystal plane, forming triangular nanosheets with a thickness of

7.82 nm, as shown in Figure 3(i,iv,v). In this case, the growth process is mainly achieved through a one-step chemical reaction in which $MnCl_2$ reacts with Se vapor to directly generate vapor-phase MnSe, which preferentially crystallizes on the (111) plane. These results provide new methods and ideas for controlling the morphology and crystal plane selectivity of nanomaterials.^[41]

2.3. Substrate Regulation

In the process of CVD growth, the substrate plays a crucial role. As the foundation for material growth, the surface properties of the substrate significantly influence nucleation and growth behavior.^[118] The thermal conductivity and thermal expansion coefficient of the substrate affect temperature distribution and thermal stress during the deposition process.^[26,116] Moreover, the lattice structure of the substrate directly impacts the lattice matching with the deposited material.^[119,120] Therefore, when designing CVD experiments, it is essential to carefully consider the various properties of the substrate. Additionally, 2D magnetic films grown on different substrates can form heterostructures with the substrate, giving rise to numerous unique properties and physical phenomena that have attracted considerable interest from researchers. In this chapter, we explore in depth the impact of substrates on the CVD growth of 2D magnetic nanosheets, summarize methods for obtaining high-quality 2D crystals from the perspective of substrate properties, and discuss the application of CVD in the fabrication of 2D magnetic heterostructures, as well as the characteristics of these magnetic heterostructures.

In the study conducted by Zhang et al., the influence of substrate type on the morphology, thickness, and distribution of CVD-grown 2D FeS nanosheets was systematically investigated. Figure 4a(i),(ii) illustrate the morphology and thickness distribution of FeS nanosheets grown on SiO_2/Si substrates at 530 and 550 °C, respectively. The FeS nanosheets primarily formed a trapezoidal structure, with their thickness increasing as the temperature rose. However, the thickness distribution was relatively broad, indicating challenges in precisely controlling the thickness of FeS nanosheets on SiO_2/Si substrates. In contrast, Figure 4a(iii),(iv) show the morphology and thickness distribution of FeS nanosheets grown on WSe_2 substrates. Under the same temperature conditions, the FeS nanosheets predominantly exhibited a regular triangular morphology. More importantly, the thickness distribution was more concentrated, particularly at 530 °C, where over 80% of the nanosheets had a thickness centered ≈6 nm, demonstrating the superiority of WSe_2 substrates in achieving more uniform thickness control. This difference can be attributed to the flat and dangling-bond-free surface of the WSe_2 substrate, which reduces lattice mismatch with FeS, thereby providing more favorable growth conditions.^[121]

This conclusion is consistent with the findings of Wu et al. regarding the controlled CVD growth of Cr_5Te_8 nanosheets. Figure 4b presents a schematic diagram of Cr_5Te_8 nanosheet preparation, with the growth results shown in Figure 4c,d. Nanosheets grown on mica substrates were noticeably thinner, with a thickness of 1.2 nm and a triangular shape (Figure 4c), whereas Cr_5Te_8 nanosheets grown on SiO_2/Si substrates had a thickness of ≈6.7 nm and tended to exhibit a hexagonal shape (Figure 4d). This can be attributed to the fact that mica, similar to

WSe_2 , is an atomically smooth and dangling-bond-free substrate that provides a highly uniform and low-energy surface, facilitating the formation of ultra-thin layers and reducing the likelihood of multilayer formation, thus promoting high-quality growth of Cr_5Te_8 nanosheets. Both studies suggest that the introduction of smooth, dangling-bond-free substrates is beneficial for achieving high-quality growth of 2D magnetic nanosheets.^[26]

In addition to selecting suitable substrates to enhance the quality of nanosheet growth, introducing additional substances on the substrate surface for surface modification can also achieve this goal. For example, Luo et al. spin-coated a KOH solution onto a SiO_2/Si substrate, which significantly influenced the growth morphology and structural properties of Cr_2S_3 .^[121] The presence of KOH effectively suppressed the vertical growth of Cr_2S_3 along the [001] direction, promoting its lateral growth on the substrate surface. This effect resulted in Cr_2S_3 forming a regular hexagonal structure on the KOH-modified substrate, as shown in Figure 4e, while Cr_2S_3 grown without KOH exhibited highly irregular morphology and a pronounced tendency for vertical growth, as shown in Figure 4f. Additionally, the introduction of KOH enhanced the interface formation energy between Cr_2S_3 and the SiO_2/Si substrate. According to density functional theory (DFT) calculations, the presence of OH^- increased the formation energy of Cr_2S_3 on the SiO_2/Si substrate from 9.040 to 9.789 eV cell⁻¹, indicating that OH^- stabilized the attachment of Cr_2S_3 on the substrate surface, promoting the formation of thin-layer structures. The introduction of OH^- also effectively reduced structural distortions at the interface during Cr_2S_3 growth, further promoting the growth of more regular and uniform thin-layer Cr_2S_3 nanosheets. These results suggest that modifying the substrate with KOH is an effective strategy to regulate the growth morphology and structural properties of non-van der Waals magnetic materials, providing a feasible approach for the preparation of high-quality 2D materials.^[116]

The aforementioned studies demonstrate that substrates, serving as the foundational base for material growth in CVD processes, have a significant impact on the morphology and structure of 2D magnetic materials. Simultaneously, when 2D magnetic nanosheets are deposited onto substrate surfaces, they form specialized structures known as magnetic heterostructures. In such heterostructures, the lattice matching and surface chemical properties of the substrate markedly influence interfacial magnetic coupling and charge transfer, leading to various novel physical phenomena.^[119,120] In the following paragraphs, we will delve deeper into the application of CVD techniques in the growth of magnetic heterostructures and the emergence of moiré superlattices within these structures.

Taking the study by Wang et al. as an example, they successfully synthesized 2D $CuCr_2Te_4$ nanosheets and their heterostructures via CVD, thoroughly investigating their growth mechanisms and magnetic properties. Figure 5a illustrates a schematic of $CuCr_2Te_4$ epitaxially grown on a Cr_2Te_3 substrate through lattice matching. This diagram clearly demonstrates the excellent lattice matching between $CuCr_2Te_4$ and Cr_2Te_3 , with a lattice mismatch of less than 1%, resulting in high-quality heterostructures. Figure 5b,c presents the optical microscopy and atomic force microscopy (AFM) images of the $CuCr_2Te_4/Cr_2Te_3$ heterostructure, respectively, further confirming its successful formation and smooth surface. This heterostructure, achieved through

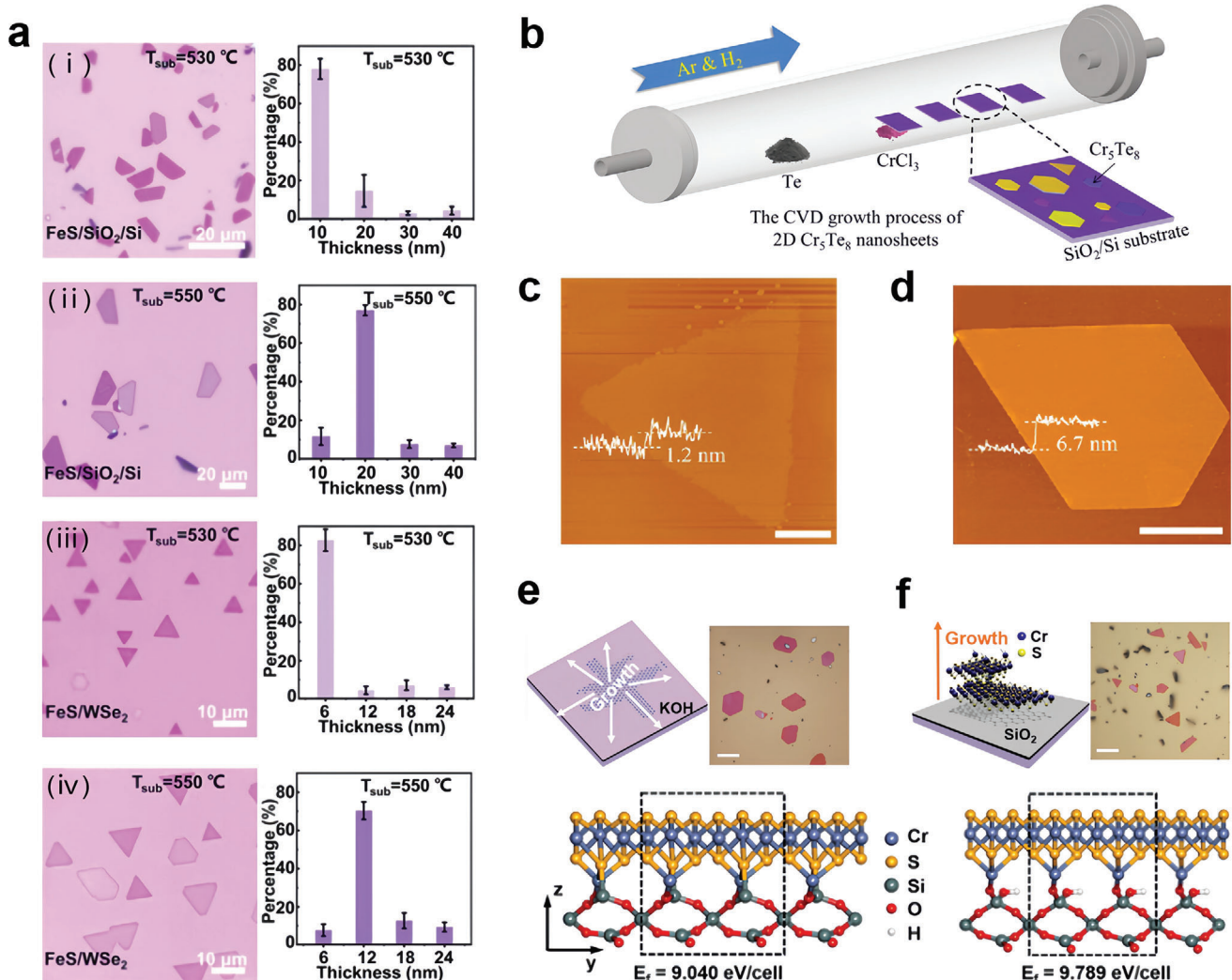


Figure 4. Substrate regulation of 2D magnetic nanosheets. a) OM images (left) and thickness histogram distributions (right) of FeS nanoplates grown on SiO₂/Si substrate at 530(i) and 550 °C(ii), respectively. OM images (left) and thickness histogram distributions (right) of FeS nanoplates grown on WSe₂ substrate at 530 (iii) and 550 °C (iv), respectively. Reproduced with permission.^[121] Copyright 2023, Elsevier. b) Schematic illustration of the CVD setup for synthesizing Cr₅Te₈ nanosheets. c,d) AFM images and corresponding height profiles of Cr₅Te₈ nanosheets grown on mica (c) and SiO₂/Si (d) substrates. Reproduced with permission.^[26] Copyright 2023, American Chemical Society. e,f) Mechanism diagrams and optical images of Cr₂S₃ growing and theoretical model of the Cr₂S₃ layer on the SiO₂ substrate with (e) or without (f) KOH. Scale bar: 10 μm. Reproduced with permission.^[116] Copyright 2022, American Chemical Society.

precise lattice-matched epitaxial growth, exhibits superior interfacial characteristics and enhanced magnetic properties. Notably, DFT calculations indicate that charge transfer at the interface is the primary contributor to the enhanced ferromagnetism observed in the CuCr₂Te₄/Cr₂Te₃ heterostructure.^[122]

Similarly, Song et al. successfully fabricated vertical Cr₂S₃/WS₂ magnetic heterostructures using two-step CVD method. Figure 5d depicts the formation process of the Cr₂S₃/WS₂ heterostructure. Initially, monolayer WS₂ is grown via CVD, followed by the deposition of Cr₂S₃ atop it, ultimately forming a high-quality heterostructure with a well-defined interface. The OM image (Figure 5e) indicates that the Cr₂S₃ nanosheets are uniformly covering the WS₂ monolayer, forming

the intended heterostructure. The AFM image (Figure 5f) shows that the thickness of the Cr₂S₃ layer is ≈2.3 nm, corresponding to a single unit cell thickness. In this study, the CVD technique facilitated the high-quality growth of the Cr₂S₃/WS₂ heterostructure through a two-step reaction process. The precise control of the Cr₂S₃ thickness achieved by adjusting growth conditions. This precise control is of great significance for investigating the electronic, magnetic, and ferroelectric properties of such heterostructures.^[119]

Furthermore, the formation of moiré superlattices was observed within the Cr₂S₃/WS₂ heterostructures.^[119] As shown in Figure 5g, high-angle annular dark-field scanning transmission electron microscopy (HAADF-STEM) images at atomic

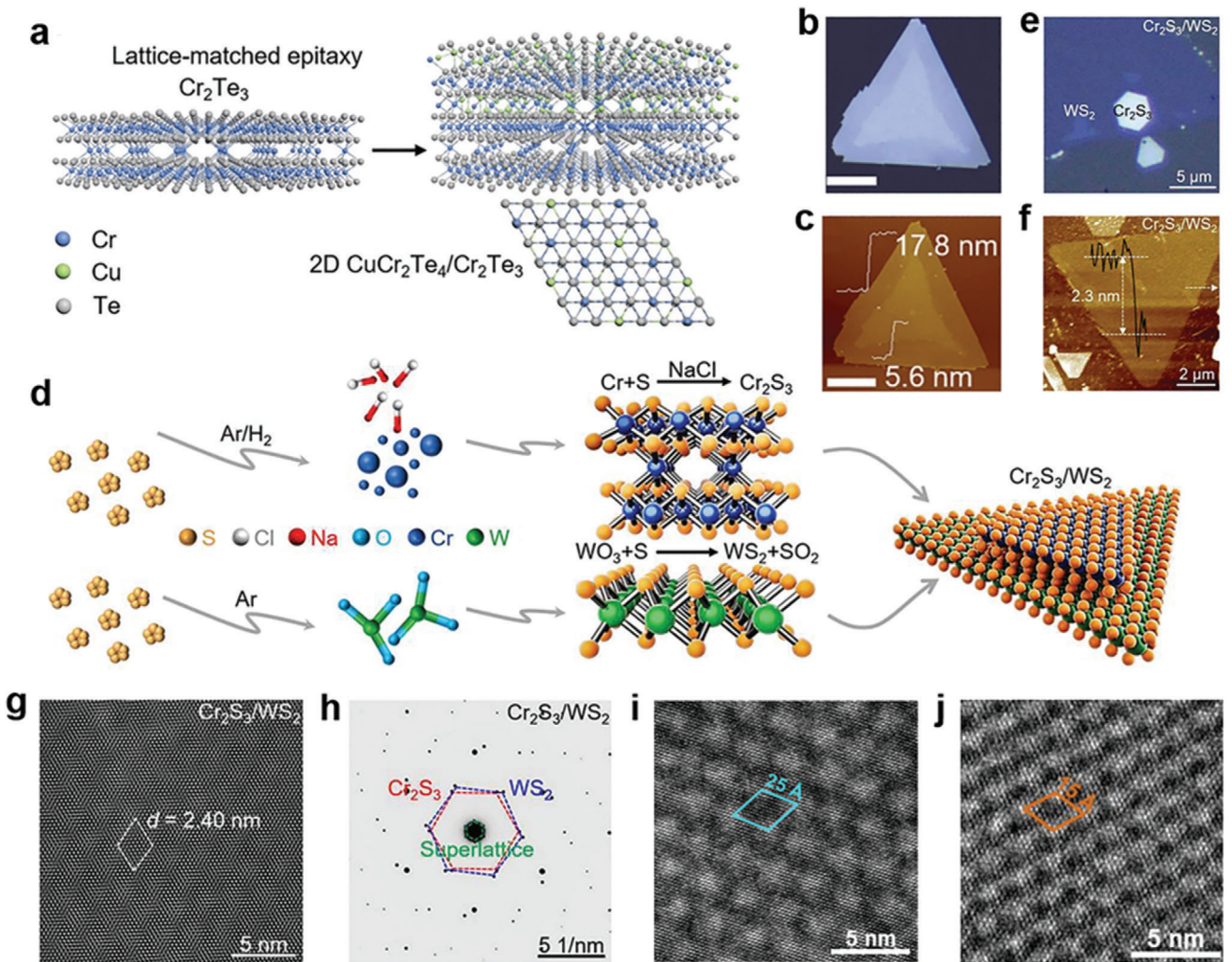


Figure 5. Magnetic heterostructures synthesized via CVD. a) Synthesis and structure schematic diagram of 2D CuCr₂Te₄/Cr₂Te₃ heterostructure. b) Optical image of CuCr₂Te₄/Cr₂Te₃ heterostructure on mica substrate. c) AFM image of a CuCr₂Te₄/Cr₂Te₃ heterostructure with thickness of bottom Cr₂Te₃ layer \approx 17.8 nm and top CuCr₂Te₄ layer \approx 5.6 nm. Reproduced with permission.^[122] Copyright 2023, Wiley-VCH GmbH. d) Schematic diagram of the growth process of Cr₂S₃/WS₂ vertical heterostructures on c-plane sapphire. e) OM image of a Cr₂S₃/WS₂ vertical heterostructures on c-plane sapphire. f) AFM image and corresponding height profile of a Cr₂S₃ nanosheet grown on monolayer WS₂ with a thickness of 2.3 nm. g) Atomic-resolution HAADF-STEM image of Cr₂S₃/WS₂ vertical heterostructures \approx 2.40 nm period moiré pattern. h) SAED pattern of a Cr₂S₃/WS₂ vertical heterostructure with the lattices of WS₂ and Cr₂S₃ and moirésuperlattice highlighted by the blue, red, and green hexagons, respectively. Reproduced with permission.^[119] Copyright 2024, American Chemical Society. i) HRTEM image of Cr₅Te₈/graphene heterostructure with \approx 25 Å period moiré pattern. j) HRTEM image of Cr₅Te₈/h-BN heterostructure with \approx 15 Å period moiré pattern. Reproduced with permission.^[120] Copyright 2022, American Chemical Society.

resolution clearly reveal a moiré superlattice with a periodicity of 2.40 nm. This periodic pattern arises from the lattice mismatch and twist angle between the Cr₂S₃ and WS₂ layers. Selected area electron diffraction (SAED) patterns (Figure 5h) display multiple sets of diffraction spots corresponding to the lattice structures of WS₂, Cr₂S₃, and the superlattice, indicating rotational misalignment during Cr₂S₃/WS₂ stacking and further confirming the existence of the moiré superlattice.^[119] The occurrence of moiré superlattices is not incidental. Jin et al. observed similar structures in magnetic heterostructure such as Cr₅Te₈/graphene and Cr₅Te₈/h-BN, with periodicities of 2.5 (Figure 5i) and 1.5 nm (Figure 5j), respectively. The presence of moiré superlattices

introduces additional periodic structures within magnetic heterostructures, modulating the crystal periodicity and magnetic interactions, thereby profoundly influencing the magnetic properties of the heterostructures.^[120]

These studies collectively underscore the critical role of substrates in influencing the growth and properties of 2D magnetic materials during CVD processes. The strategic selection and modification of substrates, along with the controlled formation of moiré superlattices, provide effective avenues for tailoring the structural and magnetic properties of 2D materials, paving the way for advanced applications in spintronics and quantum information technologies.

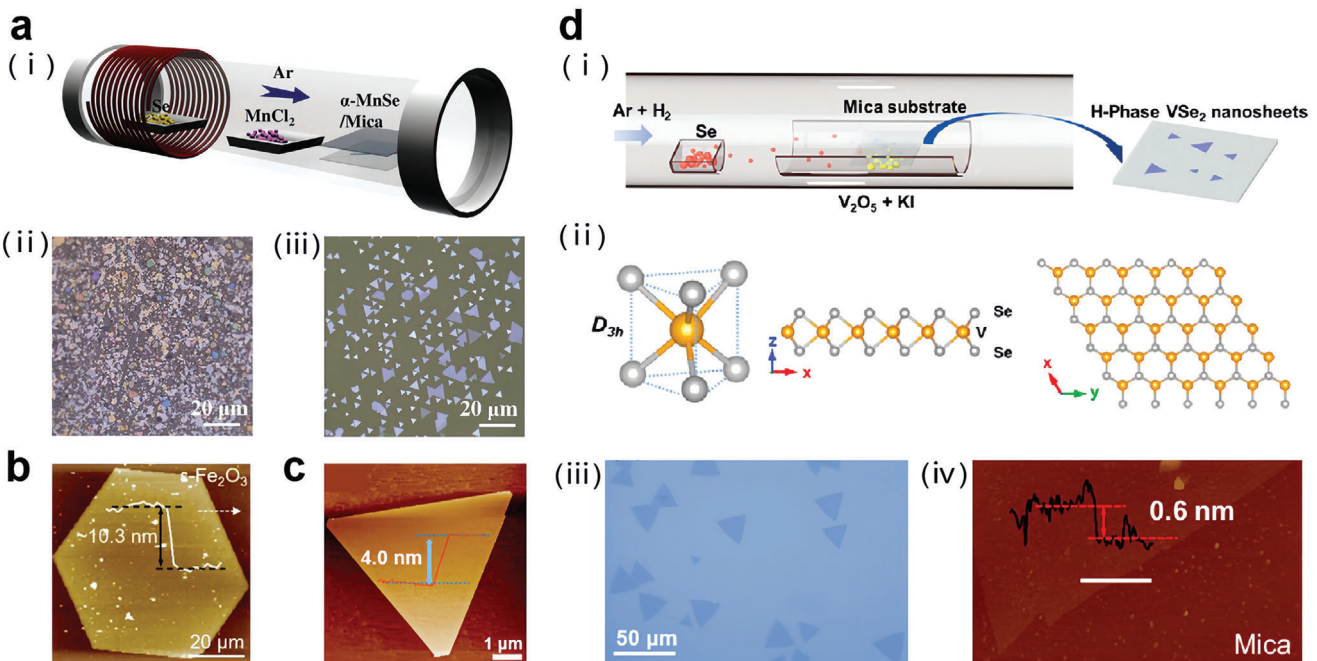


Figure 6. Shows the synthesis of 2D nanosheets through space-confined CVD and salt-assisted CVD. a) (i) Schematic illustration of a space-confined CVD setup for synthesizing ultrathin 2D α -MnSe flakes. (ii, iii) Optical images of α -MnSe flakes grown on mica without(ii)/with(iii) space-confined environment. Reproduced with permission.^[40] Copyright 2022, The Authors. Advanced Science published by Wiley-VCH GmbH. b) AFM image and corresponding height profile of $e\text{-Fe}_2\text{O}_3$ flakes grown on mica with a thickness of 10.3 nm. Reproduced with permission.^[63] Copyright 2022, Wiley-VHC GmbH. c) AFM image and corresponding height profile of 2D Fe single-crystal flakes with a thickness of 4.0 nm. Reproduced with permission.^[112] Copyright 2022, Elsevier. d) (i) Schematic illustration of a salt-assisted CVD setup for synthesizing ultrathin H-phase VSe₂ flakes. (ii) Crystal structure of H-phase VSe₂. (iii) OM image of ultrathin H-phase VSe₂ flakes. (iv) AFM image and corresponding height profile of a H-phase VSe₂ nanosheet with a thickness of 0.6nm. Reproduced with permission.^[124] Copyright 2022, American Chemical Society.

2.4. Other Factors

In the previous section, we summarized various control factors in the CVD growth of 2D magnetic materials, such as growth parameters, precursor sources, and substrates. However, these factors alone cannot fully control the CVD growth process of 2D magnetic materials. In this section, we summarize some additional influencing factors.

To date, many 2D magnetic materials have been successfully synthesized through various CVD procedures, such as direct growth CVD, salt-assisted CVD, space-confined CVD, CVD growth with pre-treated precursors, and others.^[82,123] For example, Zhou et al. successfully synthesized 2D magnetic nanosheets of α -MnSe using a space-confined CVD method, with a schematic diagram of the experimental setup shown in Figure 6a(i). In this setup, two mica sheets were stacked vertically to create an interlayer space. In this localized environment, the concentration of the precursor was significantly reduced, thereby inhibiting vertical growth and promoting the lateral growth of ultra-thin α -MnSe single crystals. Figure 6a(ii) show the α -MnSe sheets grown on mica substrates without using the space-confined strategy, while Figure 6a(iii) shows with it. As can be seen from the figures, under space-confined conditions, the thickness of the sheets is significantly reduced, and the shape is more uniform.^[40] Similarly, many high quality 2D magnetic nanoflakes are also synthesized successfully with space-confined strategy,

like $e\text{-Fe}_2\text{O}_3$ ^[63] and 2D Fe single-crystal flakes^[112] shown in Figure 6b,c.

In addition, You et al. synthesized 2D magnetic nanosheets of H-phase VSe₂ using salt-assisted CVD. The experimental setup is illustrated in Figure 6d(i). By introducing adjuvant, KI into the precursor source V₂O₅, the melting point of V₂O₅ is significantly lowered. This reduces the reaction temperature, increases the material flow, and enhances the selectivity of the H-phase VSe₂, thereby promoting the growth of H-phase VSe₂. Figure 6d(iii) shows an optical microscopy image of monolayer VSe₂ nanosheets. The image reveals a large number of triangular nanosheets, indicating the successful growth of monolayer H-phase VSe₂ nanosheets under specific conditions. Figure 6d(iv) presents an atomic force microscopy (AFM) image of the VSe₂ nanosheets grown on a mica substrate. The thickness of the nanosheets is \approx 0.6 nm, consistent with the thickness of monolayer VSe₂. These two studies demonstrate that specific modifications to the CVD process can significantly improve the quality of 2D magnetic nanosheets.^[124]

Moreover, there exist many other factors greatly influencing the synthesis of 2D magnetic materials as well. For instance, Li et al. introduced Te as an auxiliary agent playing a crucial role in the synthesis of 2D ironene which were synthesized by space-confined CVD. The schematic diagram of setup is shown in Figure 7a(i). Te facilitated the volatilization of the Fe precursor by interacting with it, significantly promoting the anisotropic growth of the 2D ironene. Additionally, Te atoms preferentially

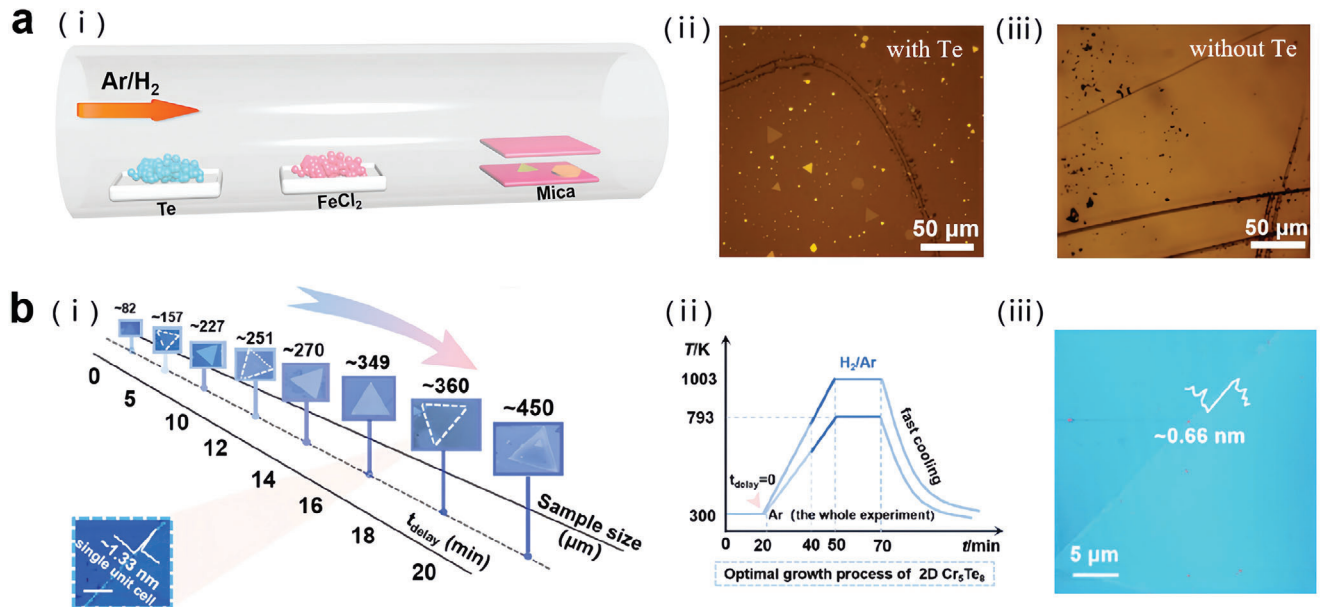


Figure 7. Shows the influence of Te and hydrogen in CVD process. a) (i) A schematic view of the Te-assisted CVD process of 2D ironene using two stacked micas as substrates for space-confined growth. (ii, iii) Optical image of the 2D Fe single-crystal flakes with (ii)/without (iii) Te powder. These two images show the effect of Te powder. Reproduced with permission.^[112] Copyright 2022, Elsevier. b) (i) Evolution of the sample size of Cr₅Te₈ nanosheets with t_{delay} . (ii) Temperature profile of the growth process of the Cr₅Te₈ nanosheets. (iii) AFM image and its corresponding height profile of an ultrathin Cr₅Te₈ triangle with a typical thickness of ≈ 0.66 nm. Reproduced with permission.^[125] Copyright 2022, American Chemical Society.

adsorbed onto the (111) plane of Fe, acting as a surface passivator. This passivation disrupted the thermodynamic equilibrium and inhibited the isotropic growth of Fe in the 3D direction, thereby encouraging the formation of the material in a 2D structure. Furthermore, the bonding between Te and the Fe surface formed a passivation layer that protected the ironene from oxidation and degradation to some extent. Through these mechanisms, the introduction of Te effectively promoted the successful growth of 2D ironene nanoflakes, which exhibit unique magnetic structures, thereby offering significant potential for future spintronic applications.^[112]

Ultimately, the composition of gases has a significant impact on the growth of nanosheets. Hydrogen, which plays a role of catalyst in various CVD growth procedures, will have a significant effect on sample growth introducing it at different times.^[125] For example, Jiang et al. studied the effect of the introduction time of hydrogen (delay time) on the lateral size of 2D magnetic nanosheets Cr₅Te₈. The experiment showed (Figure 7b(i)) that as the delay time varied from 0 to 20 min, the average size of the nanosheets increased from ≈ 80 micrometers to a maximum of about 450 micrometers. At a delay time of 16 min, the sample size was about 360 μm , and at this point, the sample thickness approached the unit cell thickness (≈ 1.33 nm). The delayed introduction of hydrogen can significantly affect the growth size of Cr₅Te₈ nanosheets, and controlling the appropriate delay time allows for the production of large-sized and ultra-thin Cr₅Te₈ nanosheets. Figure 7b(ii) shows the temperature variation curve during the growth process of Cr₅Te₈ nanosheets, illustrating the timing of hydrogen introduction at specific time points.^[125]

In conclusion, the growth parameters and conditions in the chemical vapor deposition (CVD) process have a significant impact on the morphology and functional properties of 2D magnetic materials. By optimizing these parameters, high-quality 2D magnetic materials can be obtained, laying a foundation for the development of spintronic devices.

3. Magnetic Characterization

In the previous chapter, we elaborate the key factors for the synthesis of 2D magnetic materials via CVD methods. After the successful preparation of the material, the magnetic characterization is a crucial step. However, characterization of the magnetic properties of 2D materials remains a major challenge, as strong thermal fluctuations and device manufacturing processes may rapidly destroy the magnetic properties of 2D materials. This section provides a brief review and discussion of the methods used to characterize the magnetic properties of 2D materials synthesized via CVD.

3.1. Magnetization Measurement

Vibrating Sample Magnetometer (VSM) is a mass-based magnetic characterization method that can display distinct magnetization versus magnetic field (M-H) and magnetization versus temperature (M-T) curves, revealing the total magnetic moment of the sample.^[82] The hysteresis loop observed in the M-H curve is a key indicator of ferromagnetism. By comparing the field-cooled (FC) M-T curve and the zero-field-cooled (ZFC) M-T curve,

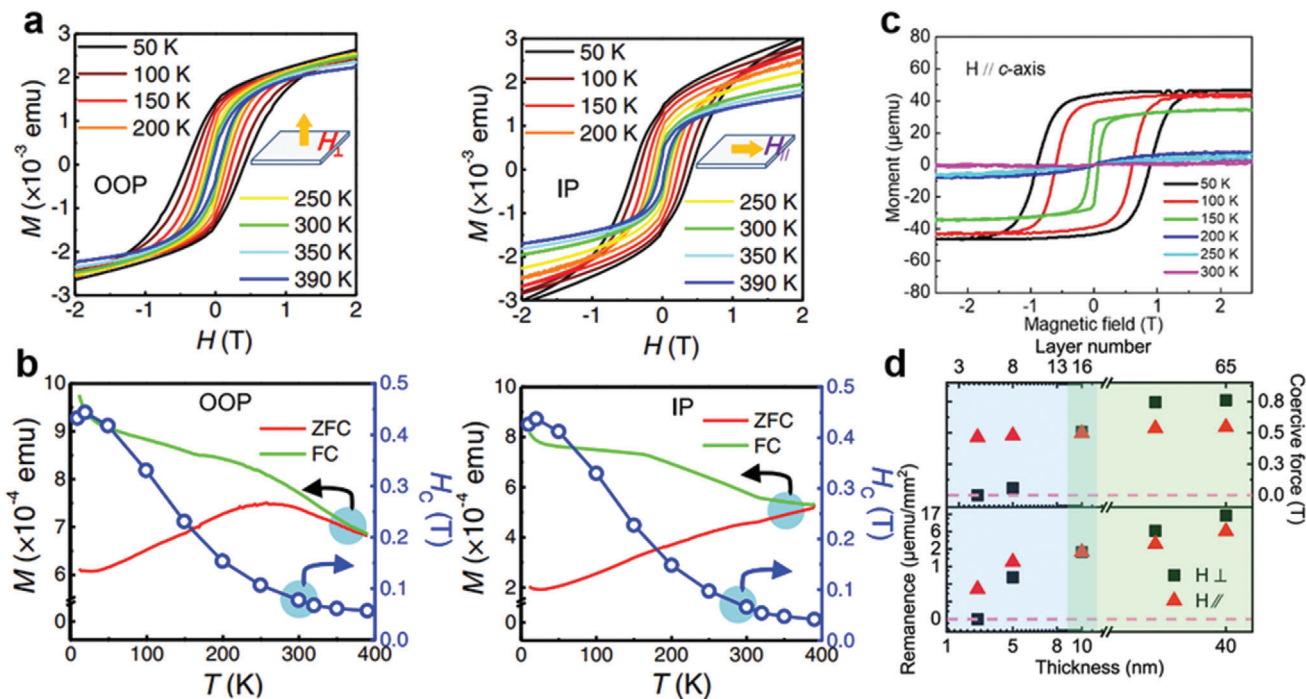


Figure 8. a) Magnetic hysteresis loops of CoFe₂O₄ nanoflakes under OOP (left) and IP (right) magnetic field at different temperatures. b) Temperature dependence of FC and ZFC magnetization curves for CoFe₂O₄ samples under OOP (left) and IP (right) magnetic field. Reproduced with permission.^[66] Copyright 2022, Springer Nature. c) Temperature-dependent magnetic hysteresis loops of 1T-CrTe₂ under the parallel magnetic field obtained by SQUID. d) Remanence and coercive force at zero field for 1T-CrTe₂ samples of various thicknesses. Reproduced with permission.^[127] Copyright 2021, Springer Nature.

the magnetic ground state of the material can be observed, and the T_c can be inferred. For instance, CoFe₂O₄ displays hysteresis loops in the M-H curves obtained from VSM measurements, confirming its ferromagnetic nature with T_c higher than room temperature and revealing magnetic anisotropy with the easy magnetization axis aligned along the in-plane (IP) direction, as illustrated in Figure 8a. Moreover, the ZFC and FC curves in Figure 8b further support this conclusion.^[66]

Moreover, there is another commonly used magnetic characterization method, Superconducting Quantum Interference Device (SQUID), with higher data accuracy compared to VSM, especially when measuring magnetic materials synthesized via CVD.^[126] Due to the limited quantity and extremely thin nature of CVD-grown 2D materials, the sample mass may be insufficient to generate a strong enough magnetic response. On the other hand, these materials are typically deposited on substrates with significantly greater mass than the ultrathin nanosheets. The magnetic impurity signals from the substrate or certain contaminants in the laboratory environment can lead to incorrect measurement of the magnetic properties of the material.^[126] Meng et al. investigated the magnetic properties of 1T-CrTe₂ nanosheets using SQUID. The magnetic hysteresis loops of 1T-CrTe₂ with a thickness of about 10 nm under a parallel magnetic field are shown in Figure 8c. They further studied the magnetic hysteresis loops of 1T-CrTe₂ with different thicknesses at 100 K, extracting the corresponding values of remanence and coercive force, and plotted Figure 8d, which summarizes the relationship between the magnetic properties of 1T-CrTe₂ and its thickness.^[127]

3.2. Magnetic Force Microscopy

The surface magnetism of 2D materials can be directly detected using Magnetic Force Microscopy (MFM). This technique, a type of scanning probe microscopy, acquires surface magnetization structures through the magnetic interactions between a magnetic probe and the sample.

As shown in Figure 9a, MFM images of Co₂Fe₆O₆ exhibit distinct magnetic domain structures as the thickness increases. For the nanoflake with a thickness ≈ 3.5 nm (Figure 9a(i)), the MFM image shows a clear single-domain structure. As the thickness increases, the magnetic structure of the nanoflakes transitions to a multi-domain configuration, shown in Figure 9a(ii),(iii), where the sample is divided into multiple magnetic domains with parallel and antiparallel magnetization, reducing magnetostatic energy. These results highlight the transition of the magnetic domain structure in Co₂Fe₆O₆ nanoflakes from single-domain to multi-domain and demonstrate the significant influence of thickness on magnetic structures.^[66] The evolution of magnetic domains is not only influenced by thickness, but the lateral size of magnetic nanosheets also plays a significant role. As shown in Figure 9b, MFM figure of γ-Fe₂O₃ nanosheets with varying lateral sizes, it is evident that as the lateral size increases, the magnetic domain structure transitions from a single-domain to a multi-domain structure.^[65]

In addition, MFM can be used to obtain topological structure images and MFM phase images, which are useful for analyzing surface structures. For example, Figure 9c displays MFM phase

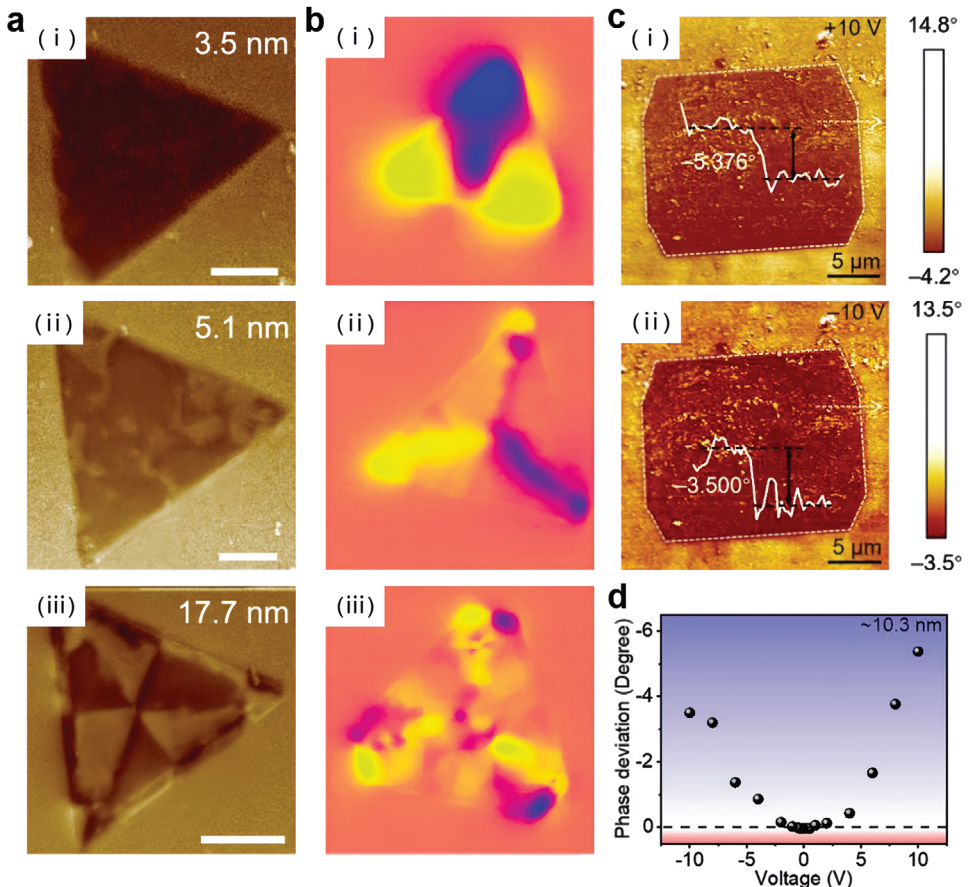


Figure 9. a) MFM phase images of $\text{Co}_2\text{Fe}_2\text{O}_6$ nanosheets with variable thicknesses (3.5 nm (i), 5.1 nm (ii), 17.7 nm (iii)) measured at room temperature. Scale bars: 3 μm . Reproduced with permission.^[66] Copyright 2022, Springer Nature. b) MFM images of $\gamma\text{-Fe}_2\text{O}_3$ nanoflakes with different lateral size: (i) small size (lateral size < 0.8 μm), (ii) medium-sized (0.8 μm < lateral size < 1.35 μm) and (iii) large-sized (lateral size > 1.35 μm) triangles. Reproduced with permission.^[65] Copyright 2023, American Chemical Society. c) MFM phase images of a rectangular $\epsilon\text{-Fe}_2\text{O}_3$ single crystal, applying the voltages of +10 (i), and -10 V (ii), respectively. d) Voltage-dependent phase deviation of the rectangular $\epsilon\text{-Fe}_2\text{O}_3$ single crystal. Reproduced with permission.^[63] Copyright 2022, Wiley-VCH GmbH.

images of $\epsilon\text{-Fe}_2\text{O}_3$ single crystals under different voltage conditions. Figure 9d shows the curve of phase shift as a function of voltage, verifying the magnetoelectric coupling phenomenon in the $\epsilon\text{-Fe}_2\text{O}_3$ sample.^[63]

3.3. Magneto-Optical Measurements

Magneto-optical effects are effective tools for precisely revealing magnetically ordered structures. Among them, Magneto-Optical Kerr Effect (MOKE) and Reflective Magnetic Circular Dichroism (RMCD) have been widely used to probe the magnetism of large-scale 2D ultrathin magnets.^[18,19,66] These measurements not only detect magnetic signals but also map the spatial distribution of signal intensity, thereby revealing the uniformity of the magnetic order. In addition to their high precision and fast measurement capabilities, magneto-optical measurements offer non-contact and non-destructive testing, unlike MFM, which requires direct contact with the sample surface.

A wide range of ultrathin magnetic materials have been successfully studied using these measurements. For instance,

Figure 10a shows the Kerr rotation signal of $\text{Cr}_2\text{Ge}_2\text{Te}_6$,^[18] and Figure 10b displays the Kerr rotation angle (θ_k) versus applied magnetic field ($\mu_{\text{n}}\text{H}$) curves for CrI_3 with different layer numbers, demonstrating the layer-dependent magnetic phase transitions in CrI_3 .^[19] Similarly, the magnetism of many ultrathin materials grown by CVD has also been characterized using magneto-optical measurements. For example, Figure 10c shows the MOKE hysteresis loops of $\text{Co}_2\text{Fe}_2\text{O}_6$ at varying thicknesses, as reported by Cheng et al., indicating its thickness-tunable magnetism, similar to CrI_3 . However, since $\text{Co}_2\text{Fe}_2\text{O}_6$ is a non-layered structure, its magnetism is primarily governed by strong internal 3D magnetic coupling, and as the thickness decreases, it does not exhibit the pronounced layer-dependent magnetic interactions seen in CrI_3 . Instead, its hysteresis loops deform significantly at smaller thicknesses. Figure 10d shows the trend of coercivity (H_c) as a function of $\text{Co}_2\text{Fe}_2\text{O}_6$ nanosheet thickness at cryogenic (80K), room temperature (300K), and elevated temperature (360K), with coercivity data obtained from MOKE hysteresis loops. Figure 10e,f, obtained via MOKE microscopy, demonstrate the dynamic evolution of magnetic domains in thinner and thicker $\text{Co}_2\text{Fe}_2\text{O}_6$ nanosheets. The thinner nanosheets exhibit

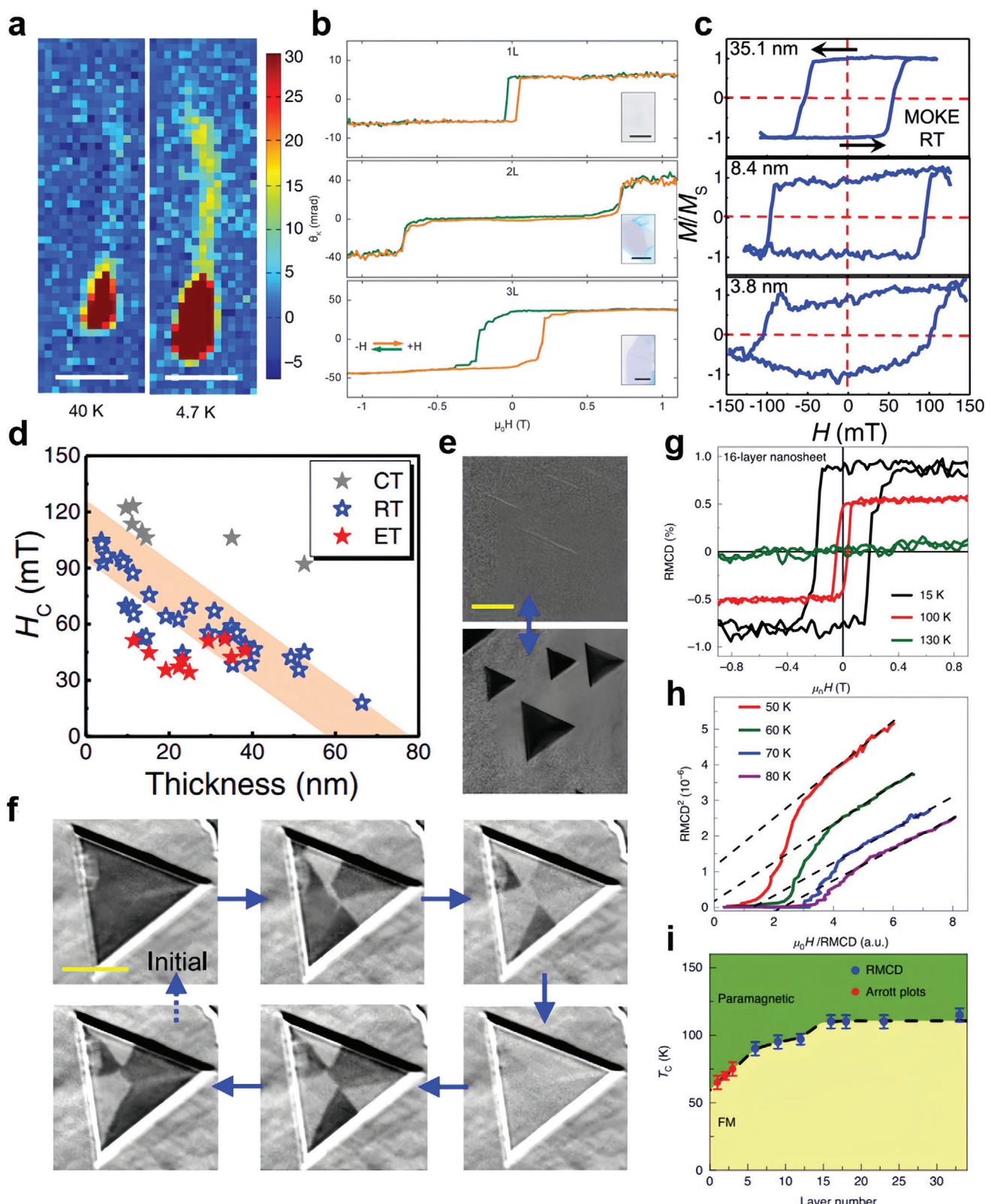


Figure 10. a) The emergence of a Kerr rotation signal for the bilayer flake under 0.075 T with the temperature at 40 K and 4.7 K. Reproduced with permission.^[18] Copyright 2017, Springer Nature. b) MOKE measured curves of CrI₃ flakes with 1, 2, and 3 layers. Reproduced with permission.^[19] Copyright 2017, Springer Nature. c) MOKE hysteresis loops of Co₂Fe₂O₆ with a thickness of 35.1, 8.4, and 3.8 nm, respectively. d) The plot of H_c versus the thickness of Co₂Fe₂O₆ nanosheets at cryogenic temperature (CT, 80 K), RT, and elevated temperature (ET, 360 K), respectively. e,f) MOKE and TEM images of a triangular nanosheet.

microscopy images of typical thin (d) and thick (e) $\text{Co}_2\text{Fe}_2\text{O}_6$ nanosheets during the magnetization reversal at room temperature. Reproduced with permission.^[66] Copyright 2022, Springer Nature. g) Polar RMCD signals of the 16-layer CrSe_2 nanosheet at different temperatures. h) Arrott plots of the RMCD data of the CrSe_2 monolayer. i) Magnetic phase diagram for CrSe_2 of layer number versus temperature. Reproduced with permission.^[108] Copyright 2021, Springer Nature.

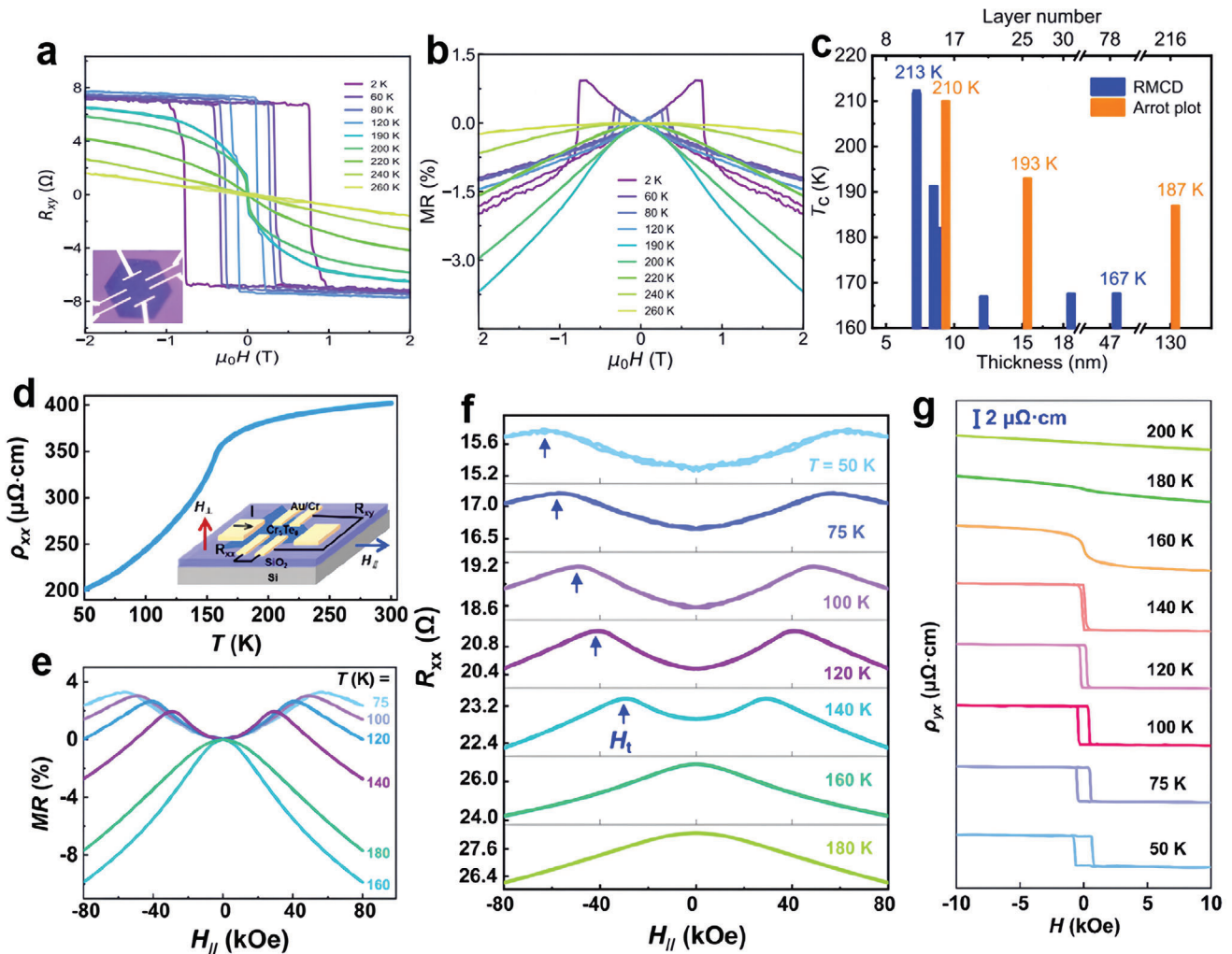


Figure 11. a,b) Out-of-plane Hall resistance hysteresis loops and magneto resistance of 10.0 nm thick 1T-Cr Te_2 device. Inset: OM image of the corresponding Hall device. c) The trend of T_c as a function of thickness of 1T-Cr Te_2 . Reproduced with permission.^[127] Copyright 2021, Springer Nature. d) Temperature-dependent resistivity of the 32 nm thick Cr_5Te_8 sample. Inset shows the schematic of the Hall bar device. e) MR of Cr_5Te_8 device at various temperatures. f) Field-dependent in-plane magnetoresistance of Cr_5Te_8 device at various temperatures. g) Hall resistance hysteresis loops of Cr_5Te_8 at various temperatures. Reproduced with permission.^[125] Copyright 2024, American Chemical Society.

a single magnetic domain with a uniform magnetization reversal process, while the thicker nanosheets display multi-domain structures where the domain flipping is uneven, resulting in segmented magnetization reversal. This behavior corresponds to what is shown in Figure 9b.^[66]

Another outstanding magneto-optical characterization technique, RMCD, has also made a remarkable impact in the field of magnetic characterization. For instance, Figure 10g shows the RMCD signals of a 16-layer CrSe_2 nanosheet at different temperatures, displaying clear hysteresis loops, indicating the presence of out-of-plane ferromagnetic order. Figure 10h presents the arrott plot for the CrSe_2 monolayer, which is generated based on

RMCD measurement data. This is used to analyze and determine the ferromagnetic behavior and T_c of the CrSe_2 monolayer, which is ≈ 65 K. Figure 10i summarizes the T_c at different thicknesses and presents the magnetic phase diagram of CrSe_2 nanosheets, showing the relationship between layer number and T_c .^[108]

3.4. Magnetotransport

Magnetoelectric measurements can reveal the magnetism of individual nanosheets with specific morphology and thickness, and their magnetic origins can also be elucidated through magnetic transport properties. By conducting magnetic transport

measurements on individual nanosheets with specific thicknesses, the specific magnetism can be determined. Therefore, the intrinsic magnetism of 2D materials can be successfully revealed through their magnetic transport performance.

The variation of the transverse resistance (R_{xy}) of CrTe₂ nanosheets with the applied magnetic field ($\mu_0 H$) is shown in Figure 11a. The distinct hysteresis loop observed at low temperatures indicates the presence of a strong anomalous Hall effect (AHE) in the material, which is characteristic of ferromagnetic order. Figure 11b depicts the variation of magnetoresistance (MR) with the applied magnetic field ($\mu_0 H$). The butterfly-shaped MR curve, caused by spin-flip phenomena under specific magnetic fields, is particularly evident at low temperatures, further confirming its low-temperature magnetism.^[127]

Similarly, spin-flip phenomena were also observed in the MR-H curves of Cr₅Te₈ nanosheets, as shown in Figure 11e. Figure 11f displays the temperature-dependent non-monotonic behavior of longitudinal resistance R_{xx} with the magnetic field, which is related to the dynamics of magnetic domain walls and spin alignment within the material, affecting the resistance. Figure 11g shows the variation of ρ_{xx} with the magnetic field at different temperatures, demonstrating AHE in Cr₅Te₈ nanosheets. The curves below T_c exhibit clear hysteresis loops and distinct switching edges, reflecting the ferromagnetic order and perpendicular magnetic anisotropy within the material.^[125]

4. Applications of 2D Magnetic Materials

4.1. Spintronic Devices

Compared to conventional electronic devices that rely on electron transport in semiconductor materials, spintronics consume significantly less energy due to low-power spin dynamics.^[128] This substantial reduction in energy consumption, often by several orders of magnitude, greatly increases the density of information processing and meets the demands of an era where silicon-based electronic devices are approaching their limits.^[20] The extraordinary properties of 2D magnetic materials make them particularly promising for applications in spintronic devices.^[126]

By leveraging electrical means to control spin-orbital degrees of freedom, namely magnetization switching, we can achieve simultaneous transport of charge and spin.^[129] Various spintronic devices, such as spin valves, spin-orbit torque devices, and 2D magnetic tunnel junctions (MTJs), have been successfully implemented using 2D magnetic materials.^[130] This review will primarily focus on these spintronic device applications of 2D magnetic materials.

4.1.1. Magnetic Tunnel Junctions

Magnetic Tunnel Junctions (MTJs) are key spintronic devices with wide applications in magnetic storage and sensing technologies.^[131] The basic structure of an MTJ consists of two ferromagnetic layers separated by an ultrathin insulating layer. Its operation is based on quantum tunneling and spin-dependent transport.^[132] Electrons can tunnel through the insulating barrier due to the quantum tunneling effect, with the tunneling probability depending on the relative magnetization directions of the two ferromagnetic layers.^[133]

When the magnetizations are parallel, the tunneling probability is higher, resulting in lower resistance. Conversely, when they are antiparallel, the tunneling probability is lower, leading to higher resistance. This phenomenon is known as the Tunnel Magnetoresistance (TMR) effect.^[132] In recent years, significant improvements in MTJ performance have been achieved through optimization of materials and structures, paving the way for applications in technologies such as Magnetic Random Access Memory (MRAM).^[134]

The performance of MTJs is mainly determined by the TMR ratio and the switching field strength. Due to thermal stability issues and scale effects in traditional magnetic films, maintaining a high TMR ratio becomes challenging. 2D magnetic materials perfectly address these issues.^[135] Song et al. designed and fabricated a novel spin-filter MTJ structure using atomically thin CrI₃ as a spin-filter tunnel barrier and graphene as electrodes.^[85] They investigated TMR by varying the number of CrI₃ layers (bilayer, trilayer, four-layer) and found that the TMR ratio increased significantly with increasing CrI₃ layers, reaching a record 19 000% for the four-layer structure at low temperatures. This remarkable result revealed that the intrinsic layer-by-layer antiferromagnetic coupling in CrI₃ is key to producing the giant TMR, with each CrI₃ layer acting as a spin filter.

However, the low T_c (≈ 50 K) of CrI₃ limits its practical device application. It is urgent to find intrinsic 2D magnetic materials with high Curie or Néel temperatures for room-temperature MTJ devices. Fe₃GaTe₂ has recently been reported as a metallic 2D room-temperature ferromagnetic material with a bulk T_c of ≈ 380 K and perpendicular magnetic anisotropy (PMA).^[136] Based on the significant properties of Fe₃GaTe₂, Jin et al. fabricated Fe₃GaTe₂/WS₂/Fe₃GaTe₂ MTJ devices, achieving a remarkable tunneling magnetoresistance (TMR) ratio of up to 213% at 10 K, which persists at 11% at room temperature.^[137] Notably, they reported a high spin polarization of 72% for Fe₃GaTe₂, the highest among Fe₃GaTe₂-based all-2D van der Waals spin valves to date. The study also explored the dependence of TMR on the WS₂ barrier thickness and demonstrated the ability to reverse TMR polarity through bias current modulation.(Figure 12)

4.1.2. Spin Valves

Spin valves have emerged as a crucial component in spintronics research and applications over the past few decades.^[138] These multilayer structures, typically consisting of two ferromagnetic layers separated by a non-magnetic spacer, exploit the giant magnetoresistance (GMR) effect to control electron transport through manipulation of magnetic orientations.^[139,140]

Recent research has focused on optimizing material systems, exploring novel structural designs, investigating spin dynamics, and expanding applications beyond traditional magnetic read heads.^[140] While significant progress has been made in enhancing GMR ratios, thermal stability, and sensitivity, challenges remain in further improvements in performance metrics and reliability for emerging applications.^[141]

The performance of spin valves is determined by several key factors, including the spin polarization of the ferromagnetic electrodes, the quality of interfaces, and the spin transport properties of the spacer layer, which coincides with the

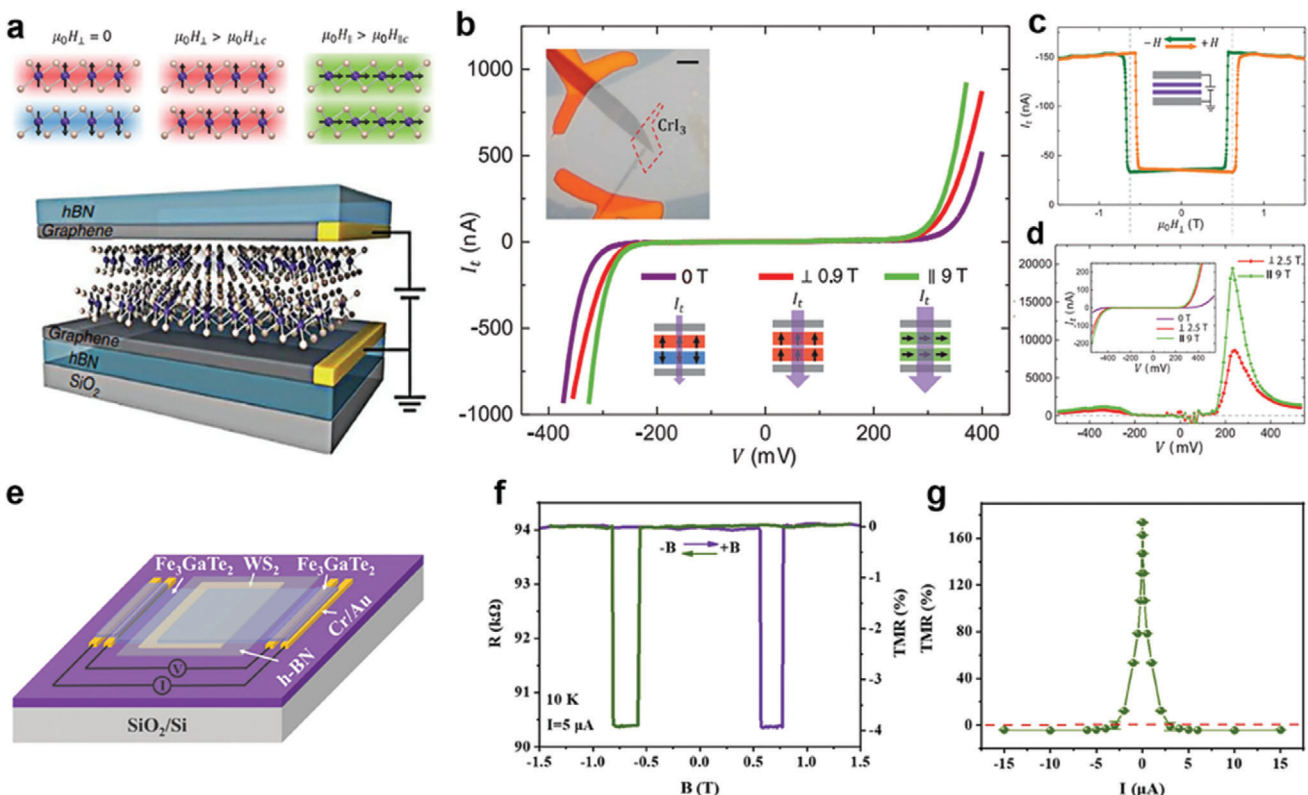


Figure 12. a) Schematic of magnetic states in bilayer CrI₃ and Schematic of 2D spin-filter magnetic tunnel junction (sf-MTJ). b) Tunneling current of a bilayer CrI₃ sf-MTJ at selected magnetic fields. (Top inset) Optical microscope image of the device (scale bar, 5 mm). c) Tunneling current as a function of out-of-plane magnetic field ($\mu_0 H_{\perp}$) at a selected bias voltage (-290 mV). d) sf-TMR ratio calculated from the I_t -V data shown in the inset. Reproduced with permission.^[136] Copyright 2022, Springer Nature. e) Schematic diagram of the Fe₃GaTe₂/WS₂/Fe₃GaTe₂ MTJs. f) Magnified TMR curve of Fe₃GaTe₂/WS₂/Fe₃GaTe₂ MTJs measured with a bias current of 5 μA . (g) I-dependent TMR ratio variations for the Fe₃GaTe₂/WS₂/Fe₃GaTe₂ MTJ. Reproduced with permission.^[137] Copyright 2023, American Chemical Society.

advantages of 2D magnetic materials.^[142] Gao et al. fabricated Cr_{1-x}Te/Al₂O₃/Cr_{1-x}Te spin valves without encapsulation, leveraging the air stability and ALD compatibility of CVD-grown Cr_{1-x}Te.^[143] They achieved a high magnetoresistance ratio of 28% at 2 K and demonstrated tunable performance by varying the Al₂O₃ barrier thickness. The ability to precisely control layer thickness and interface quality in these 2D systems allows for optimized spin-dependent transport.

Spin valves can also be constructed in lateral structures. Zhao et al. demonstrated a lateral spin valve using Fe₅GeTe₂/graphene heterostructures, achieving efficient room-temperature spin injection, transport, and detection.^[144,145] Their device exhibited multidirectional spin polarization, showcasing the potential of 2D magnets for tailoring spin injection. Additionally, spin valves with an FGT/FGT structure without a spacer layer have also been developed in recent years.^[146] (Figure 13)

4.1.3. Spin Field-Effect Transistors

The concept of spin field-effect transistors (Spin FETs) was first proposed by Datta and Das in 1990.^[147] Unlike conventional transistors, Spin FETs rely on spin operation, potentially offering higher performance in non-volatile memory devices and high-

density storage applications, and providing new opportunities for the development of spin logic devices.^[148,149]

In recent years, numerous studies have focused on constructing spin transistors based on van der Waals (vdW) heterostructures.^[150,151] For instance, Zhang et al. predicted a 2H-VSe₂-based Spin FET through DFT calculations on VSe₂.^[152] As an A-type vdW antiferromagnetic semiconductor, bilayer 2H-VSe₂ exhibits ferromagnetic (FM) coupling within layers and antiferromagnetic (AFM) coupling between layers.^[153]

Spin-tunneling FETs, which combine the characteristics of Spin FETs and spin-filter magnetic tunnel junctions (MTJs), offer more promising applications than Spin FETs alone. A significant advancement in spin-tunneling FETs based on 2D vdW materials was reported in 2019 with devices based on dual-gated Gr/CrI₃/Gr tunnel junctions.^[154] The device consists of a Gr/CrI₃/Gr vertical structure with top and bottom gates, where the middle CrI₃ (2–4 layers thick) serves as a magnetic tunnel barrier.

Taking bilayer CrI₃ as an example, the device has two simple magnetization configurations, where bilayer CrI₃ can be controlled to exhibit interlayer ferromagnetic or antiferromagnetic coupling via gate voltage. This Gr/CrI₃/Gr heterostructure-based spin-tunneling FET allows electrical control of interlayer

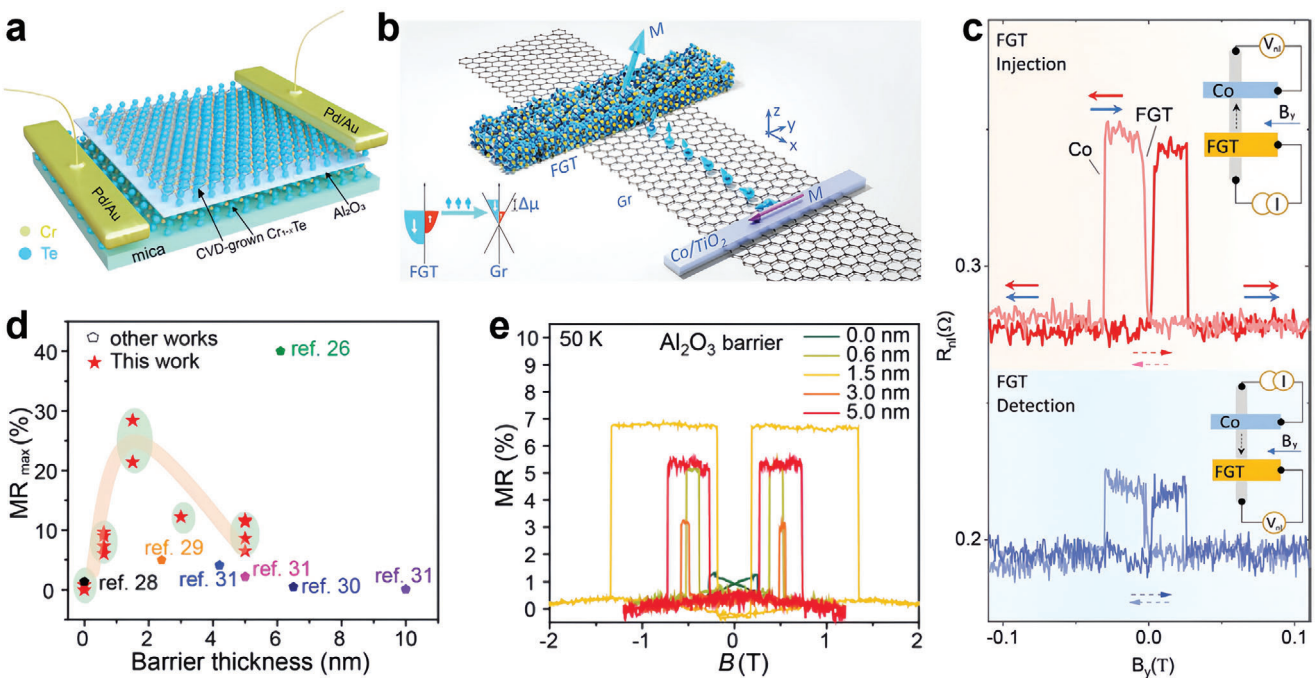


Figure 13. a) Schematic illustration and TEM characterization of Cr_{1-x}Te/Al₂O₃/Cr_{1-x}Te vertical spin valve devices. Reproduced with permission.^[143] Copyright 2022, The Authors. Advanced Electronic Materials published by Wiley-VCH GmbH. b) Schematic of a spin-valve device with FGT on a graphene (Gr) channel with reference Co/TiO₂ electrode. c) The measured nonlocal (NL) spin-valve signal $R_{nl} = V_{nl}/I_{dc}$ for spin injection from FGT with parallel (P) and antiparallel (AP) alignment of FGT and Co electrodes (red and blue arrows). Reproduced with permission.^[145] Copyright 2023, The Authors. Advanced Materials published by Wiley-VCH GmbH. d) The statistic for the observed MR magnitude of different Cr_{1-x}Te/Al₂O₃/Cr_{1-x}Te magnetic heterostructures as a function of barrier thickness of Al₂O₃. e) Al₂O₃ spacer thickness-dependent MR–B curves at 50 K, which evolved from sharp and rectangular resistance switching to a butterfly-like hysteresis when the spacer thickness decreases to 0.0 nm. Reproduced with permission.^[143] Copyright 2022, The Authors. Advanced Electronic Materials published by Wiley-VCH GmbH.

magnetic order for writing operations and utilizes the spin filtering effect for reading operations. (Figure 14)

4.1.4. Quantum Computing and Sensors

2D magnetic materials, particularly those based on topologically protected structures such as skyrmions, have emerged as promising candidates for applications in quantum computing. The unique properties of these materials, including their high surface-to-volume ratios, ease of manipulation, and tunability, make them particularly well-suited for applications that demand flexibility, scalability, and robustness.

In the realm of quantum computing, 2D magnetic materials, specifically skyrmion-based systems, offer significant advantages due to their topological protection. This protection enhances the stability of quantum bits (qubits), making them more resilient to external perturbations and reducing the effects of decoherence. The framework proposed by Christina Psaroudaki et al. introduces two primary types of skyrmion-based qubits: the Sz qubit and the helicity qubit, as shown in Figure 15a.^[155] These qubits can be effectively controlled using external parameters such as microwave fields and magnetic field gradients, enabling the realization of quantum gate operations. Furthermore, the multi-qubit coupling mechanism facilitated by nonmagnetic spacer layers allows for flexible control of both transverse and longitudinal interactions, which are essential for complex quantum op-

erations. This research highlights the potential of 2D magnetic materials as a platform for scalable quantum computing, emphasizing their ability to achieve robust and efficient quantum operations.

Beyond quantum computing, 2D ferromagnetic materials show considerable promise for use in sensing technologies. Their magnetic properties can be finely tuned to suit a variety of applications, including nanoscale memories, magnetic sensors, transparent magnets, and magneto-optic modulators. The unique combination of magnetism and flexibility in 2D ferromagnetic materials makes them ideal for use in next-generation flexible and stretchable sensors. These sensors, which require high sensitivity and compactness, benefit from the ability to control the material's magnetic properties with precision. W. Zhu et al. focus on a heterostructure consisting of 2D ferromagnetic metal Fe₃GaTe₂ and the p-type semiconductor WSe₂ (Figure 15b), achieving robust magneto-photoresponse at room temperature. The interplay between magnetism and photoelectric properties is realized via a magneto-band structure effect, where the magnetization direction modulates charge transfer and Schottky barriers at the Fe₃GaTe₂/WSe₂ interface. This allows precise and multidimensional tuning of photocurrent using magnetic fields. Such 2D optoelectronic devices surpass traditional phototransistors by enabling gate-free architectures and in-sensor vision systems, significantly improving recognition accuracy in low-contrast environments.^[156] The study demonstrates the potential of 2D magnetic materials in revolutionizing sensor technology

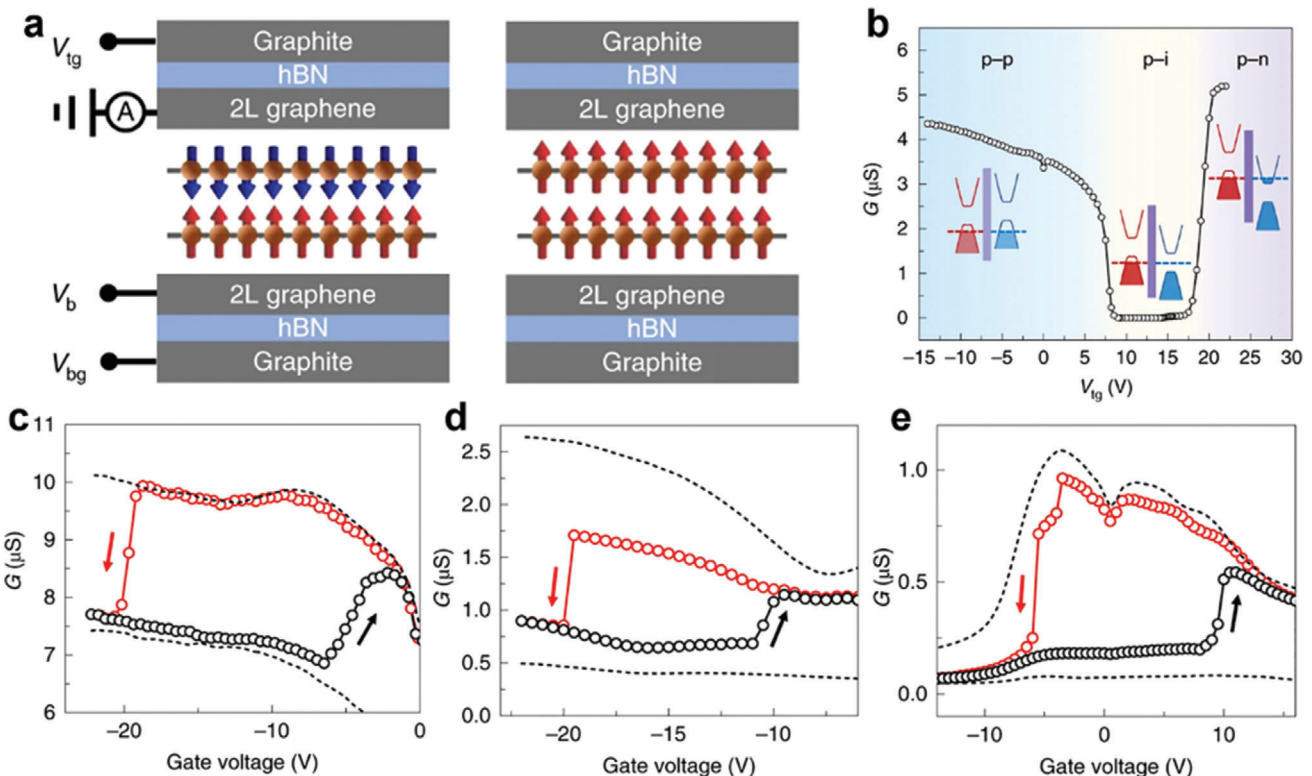


Figure 14. a) Operational principle of a spin-TFET based on a gate-controlled spin-flip transition in bilayer CrI₃ and spin filtering in the tunnel junction. b) Gate dependence of tunnel conductance shows p–p, p–i and p–n regions for device 1. c) Tunnel conductance of a TFET with a bilayer CrI₃ tunnel barrier is repeatedly switched by gating under a constant magnetic bias of 0.76 T. d) The same as in a for a TFET with a three-layer CrI₃ tunnel barrier under a constant magnetic bias of 1.7 T. e) The same as in a for a TFET with a four-layer CrI₃ tunnel barrier under a constant magnetic bias of 1.77 T. Reproduced with permission.^[154] Copyright 2019, Springer Nature.

by offering fast, contactless, and robust modulation capabilities, paving the way for bioinspired machine vision systems and multifunctional optoelectronic devices.

5. Conclusion and Perspective

2D magnetic materials have attracted widespread attention due to their unique properties and potential applications in spintronic devices. Research on 2D magnetic materials is not only crucial for understanding the mechanisms of low-dimensional magnetism but also plays an important role in promoting the development of next-generation atomic-scale spintronic devices. In the field of fabricating 2D magnetic nanosheets, CVD has proven to be a versatile and efficient synthesis technique. This review systematically discusses the effects of growth parameters such as temperature, time, and gas flow rate on the preparation of 2D magnetic materials and analyzes the regulatory impact of optimizing precursor sources and substrate conditions. Additionally, the article comprehensively summarizes recent advances in the synthesis, characterization, and potential applications of 2D magnetic materials. Despite significant progress in this field, many challenges remain. Based on recent studies, we outline several key issues that need to be addressed and expect to provide references and ideas for future research:

(a) **Theory of 2D magnetic materials:** Theories such as the Heisenberg model,^[157] Ising model,^[158,159] and XY model^[160] are commonly used to describe the magnetic interactions in 2D materials. These theories provide a foundation for understanding the magnetic behavior of 2D materials. However, with the continuous development of 2D materials, particularly the introduction of van der Waals materials and heterostructures, there is a growing need for a deeper theoretical understanding. With the advancement of computer technology, there have been new breakthroughs in the theory of 2D magnetism. Leveraging the powerful computational capabilities of modern computers, methods such as density functional theory (DFT) and Monte Carlo simulations can now accurately calculate and simulate the behavior of complex magnetic systems.^[161] Additionally, AI's powerful learning abilities allow for the design of materials with superior properties by analyzing and learning from existing 2D magnetic material structures.^[162] Despite significant theoretical progress with the assistance of computer has been achieved, there are still some challenges. For instance, complex models often suffer from small computational systems, accumulated errors, and a high demand for computational resources. Traditional models are subject to many approximations and theoretical limitations, which may not fully explain the complex behavior of 2D magnetism. Therefore, on one hand, there is

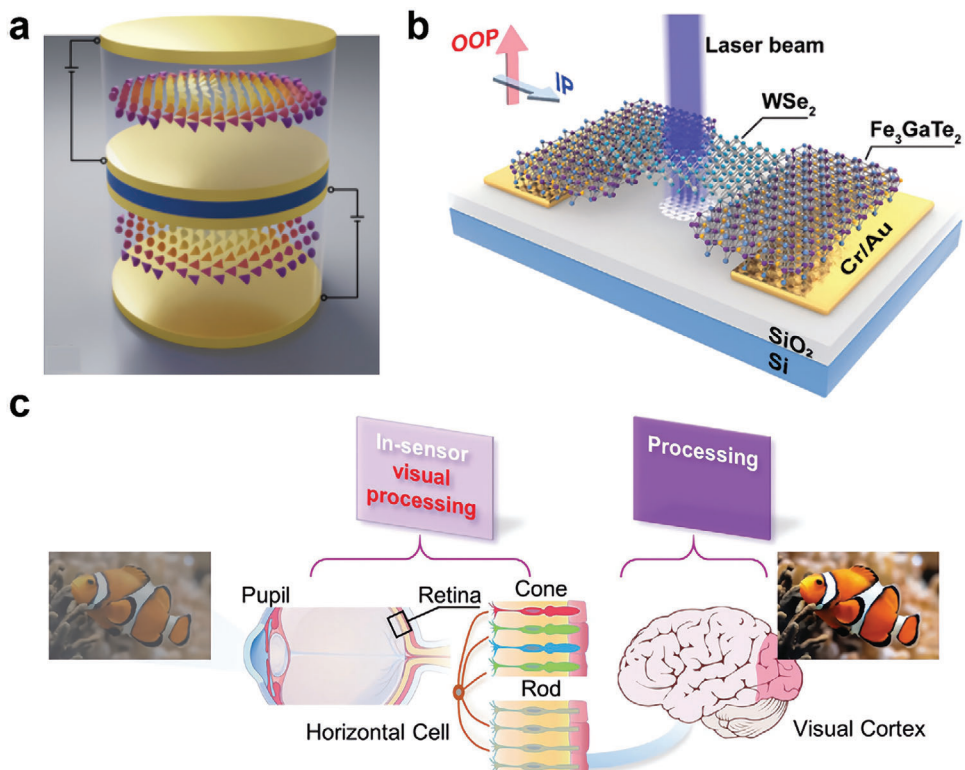


Figure 15. a) Skyrmion qubit concept based on magnetic heterostructure. Reproduced with permission.^[155] Copyright 2021, American Physical Society. b) Schematic of the optoelectronic device based on 2D magnetic material for in-Sensor vision systems shown in c). Reproduced with permission.^[156] Copyright 2024, Wiley-VCH GmbH.

a need to optimize the algorithms for 2D magnetism, and on the other hand, it is necessary to propose more advanced theoretical models.

- (b) **Insufficient experimental validation:** Theoretically, many van der Waals materials are predicted to exhibit magnetism in both 3D and 2D limits, but only a few have been experimentally verified.^[163,164] This inadequacy is particularly prominent in studies of the magnetic properties of few-layered structures compared to their bulk counterparts. Future research should focus on synthesizing more 2D magnetic materials with good reproducibility and scalability, systematically exploring the magnetic behaviors of these materials at different thicknesses to better understand the physical mechanisms of low-dimensional magnetism.
- (c) **Material stability and curie temperature:** For the practical application of 2D magnetic materials, environmental stability and T_c are major challenges. Most synthesized 2D magnetic materials exhibit poor stability under humidity, oxidation, and temperature variations, leading to degradation and reduced magnetism.^[18,19,29,38,39] Moreover, the low T_c of many 2D magnetic materials severely limit their practical use at room temperature or above.^[165] Therefore, future research should focus on developing more oxidation-resistant and environmentally stable 2D magnetic materials while striving to achieve stable magnetic phases with high T_c , thus providing

a broader platform for spintronic applications at room temperature and beyond.

- (d) **Optimization and simplification of fabrication methods:** Although existing CVD fabrication methods have shown good operability for certain systems, they still face challenges such as complex processes, poor reproducibility, and limited applicability in practical use.^[88,113] For example, while using oriented substrates for epitaxial growth of certain magnetic materials can enhance crystal quality, it may introduce additional transfer issues during device fabrication or magnetic measurements.^[45,108] Therefore, future research should focus on further optimizing existing fabrication processes, simplifying procedures, improving material preparation consistency and reproducibility, and expanding the range of applicable materials to reduce the complexity of 2D magnetic material synthesis and improve the feasibility of device manufacturing.
- (e) **Integration of heterostructures and exploration of novel properties:** Heterostructures of 2D magnetic materials exhibit many novel physical phenomena and potential application values,^[42,85,126] and direct integration of different materials through CVD is crucial for achieving high-quality heterostructures. Notably, the recently synthesized CuCr₂Te₄/Cr₂Te₃ heterostructure via the CVD method demonstrates excellent magnetic properties and

device performance, providing an ideal platform for the research and development of next-generation spintronic devices.^[122] Therefore, future research should focus on developing more heterostructures of 2D magnetic materials, systematically regulating interfacial coupling effects, and exploring new spintronic and quantum phase transition phenomena to further advance the application of 2D magnetic materials in device integration and functional control.

- (f) **Scalability of CVD processes and the integration of 2D magnetic materials into devices:** Currently, the CVD synthesis of 2D magnetic materials is usually limited to laboratory scales,^[40,54,66] making it difficult to achieve large-area uniform film growth, which severely restricts their potential for practical device applications. Key factors include controlling the nucleation and growth dynamics, minimizing defects, and optimizing deposition parameters like temperature and precursor composition. Advances in selective-area growth, heterostructure stacking, and low-temperature synthesis compatible with existing semiconductor manufacturing processes will be critical. Solving these issues would enable the integration of 2D magnetic materials into industrial-scale applications such as quantum computing and spintronic devices.
- (g) **Potential technological applications:** The future of 2D magnetic materials lies in their transformative potential across emerging technologies. In quantum computing, their topological protection and tunable spin states offer a scalable platform for fault-tolerant qubits. In spintronics, these materials promise ultra-low-power, high-speed logic devices, while their magneto-photoresponse capabilities enable advanced sensors for bioinspired vision systems and precision diagnostics. Additionally, they hold promise in energy technologies, such as magnetic thermoelectrics and spin-caloric systems, for efficient energy conversion and storage. As scalable synthesis and integration techniques advance, 2D magnetic materials are set to drive innovations across quantum information science, spintronics, and next-generation energy solutions.

In summary, although significant progress has been made in the field of 2D magnetic materials,^[113,166] their development for practical applications still faces numerous challenges. Future research should aim for breakthroughs in material synthesis, performance optimization, and device integration, thereby driving 2D magnetic materials toward real-world applications. We believe that with continuous research, 2D magnetic materials will bring more exciting and innovative applications in fields such as information storage, spintronics, and quantum computing.^[82,88]

Acknowledgements

S.Y. and Y.Z. contributed equally to this work. This work was supported by the Wuhan Industrial Innovation Joint Laboratory (no. 2024050902040443) and the Open Fund of Hubei Luojia Laboratory (no. 230100004).

Conflict of Interest

The authors declare no conflict of interest.

Keywords

2D magnetic materials, chemical vapor deposition, growth parameters, spintronic devices

Received: October 30, 2024

Revised: January 13, 2025

Published online: February 5, 2025

- [1] K. S. Novoselov, A. K. Geim, S. V. Morozov, D. Jiang, Y. Zhang, S. V. Dubonos, I. V. Grigorieva, A. A. Firsov, *Science* **2004**, *306*, 666.
- [2] M. Ramos, M. Gadea, S. Mañas-Valero, C. Boix-Constant, E. Henríquez-Guerra, M. A. Díaz-García, E. Coronado, M. R. Calvo, *Nanoscale Adv.* **2024**, *6*, 1909.
- [3] Z. Zhang, B. Zhao, D. Shen, Q. Tao, B. Li, R. Wu, B. Li, X. Yang, J. Li, R. Song, H. Zhang, Z. Huang, Z. Zhang, J. Zhou, Y. Liu, X. Duan, *Small Struct.* **2021**, *2*, 2100028.
- [4] A. Du, D. Zhu, K. Cao, Z. Zhang, Z. Guo, K. Shi, D. Xiong, R. Xiao, W. Cai, J. Yin, S. Lu, C. Zhang, Y. Zhang, S. Luo, A. Fert, W. Zhao, *Nat. Electron.* **2023**, *6*, 425.
- [5] T. S. Ghiasi, A. A. Kaverzin, A. H. Dismukes, D. K. de Wal, X. Roy, B. J. van Wees, *Nat. Nanotechnol.* **2021**, *16*, 788.
- [6] S. Niu, J. Cai, G. Wang, *Nano Res.* **2020**, *14*, 1985.
- [7] Y. Kubota, K. Watanabe, O. Tsuda, T. Taniguchi, *Science* **2007**, *317*, 932.
- [8] A. R. Jang, S. Hong, C. Hyun, S. I. Yoon, G. Kim, H. Y. Jeong, T. J. Shin, S. O. Park, K. Wong, S. K. Kwak, N. Park, K. Yu, E. Choi, A. Mishchenko, F. Withers, K. S. Novoselov, H. Lim, H. S. Shin, *Nano Lett.* **2016**, *16*, 3360.
- [9] Y. Zhang, Y. Yao, M. G. Sendeku, L. Yin, X. Zhan, F. Wang, Z. Wang, J. He, *Adv. Mater.* **2019**, *31*, 1901694.
- [10] X. Yang, J. Li, T. Liang, C. Y. Ma, Y. Y. Zhang, H. Z. Chen, N. Hanagata, H. X. Su, M. S. Xu, *Nanoscale* **2014**, *6*, 10126.
- [11] J. Li, X. D. Yang, Y. Liu, B. L. Huang, R. X. Wu, Z. W. Zhang, B. Zhao, H. F. Ma, W. Q. Dang, Z. Wei, K. Wang, Z. Y. Lin, X. X. Yan, M. Z. Sun, B. Li, X. Q. Pan, J. Luo, G. Y. Zhang, Y. Liu, Y. Huang, X. D. Duan, X. F. Duan, *Nature* **2020**, *579*, 368.
- [12] X. Feng, R. Cheng, L. Yin, Y. Wen, J. Jiang, J. He, *Adv. Mater.* **2023**, *36*, 2304708.
- [13] S. S. Cheema, N. Shanker, L. C. Wang, C. H. Hsu, S. L. Hsu, Y. H. Liao, M. San Jose, J. Gomez, W. Chakraborty, W. S. Li, J. H. Bae, S. K. Volkman, D. Kwon, Y. Rho, G. Pinelli, R. Rastogi, D. Pipitone, C. Stull, M. Cook, B. Tyrrell, V. A. Stoica, Z. Zhang, J. W. Freeland, C. J. Tassone, A. Mehta, G. Saheli, D. Thompson, D. I. Suh, W. T. Koo, K. J. Nam, et al., *Nature* **2022**, *604*, 65.
- [14] R. Z. Ma, T. Sasaki, *Acc. Chem. Res.* **2015**, *48*, 136.
- [15] R. Miranda, F. Ynduráin, D. Chandresris, J. Lecante, Y. Petroff, *Phys. Rev. B* **1982**, *25*, 527.
- [16] U. Gradmann, *Phys. Rev. B* **1983**, *27*, 1935.
- [17] J. U. Lee, S. Lee, J. H. Ryoo, S. Kang, T. Y. Kim, P. Kim, C. H. Park, J. G. Park, H. Cheong, *Nano Lett.* **2016**, *16*, 7433.
- [18] C. Gong, L. Li, Z. Li, H. Ji, A. Stern, Y. Xia, T. Cao, W. Bao, C. Wang, Y. Wang, Z. Q. Qiu, R. J. Cava, S. G. Louie, J. Xia, X. Zhang, *Nature* **2017**, *546*, 265.
- [19] B. Huang, G. Clark, E. Navarro-Moratalla, D. R. Klein, R. Cheng, K. L. Seyler, D. Zhong, E. Schmidgall, M. A. McGuire, D. H. Cobden, W. Yao, D. Xiao, P. Jarillo-Herrero, X. Xu, *Nature* **2017**, *546*, 270.
- [20] M. Gibertini, M. Koperski, A. F. Morpurgo, K. S. Novoselov, *Nat. Nanotechnol.* **2019**, *14*, 408.
- [21] K. Kim, S. Y. Lim, J. U. Lee, S. Lee, T. Y. Kim, K. Park, G. S. Jeon, C. H. Park, J. G. Park, H. Cheong, *Nat. Commun.* **2019**, *10*, 345.

- [22] H. Xiao, W. Zhuang, L. Loh, T. Liang, A. Gayen, P. Ye, M. Bosman, G. Eda, X. Wang, M. Xu, *Adv. Mater. Interfaces* **2022**, 9, 2201353.
- [23] M. Liu, C. Wu, Z. Liu, Z. Wang, D.-X. Yao, D. Zhong, *Nano Res.* **2020**, 13, 1733.
- [24] X. Zhang, Q. Lu, W. Liu, W. Niu, J. Sun, J. Cook, M. Vaninger, P. F. Miceli, D. J. Singh, S.-W. Lian, T.-R. Chang, X. He, J. Du, L. He, R. Zhang, G. Bian, Y. Xu, *Nat. Commun.* **2021**, 12, 2492.
- [25] M. Kiaba, A. Suter, Z. Salman, T. Prokscha, B. Chen, G. Koster, A. Dubroka, *Nat. Commun.* **2024**, 15, 5313.
- [26] H. Wu, J. Guo, S. Zhaxi, H. Xu, S. Mi, L. Wang, S. Chen, R. Xu, W. Ji, F. Pang, Z. Cheng, *ACS Appl. Mater. Interfaces* **2023**, 15, 26148.
- [27] W. J. Hardy, J. Yuan, H. Guo, P. Zhou, J. Lou, D. Natelson, *ACS Nano* **2016**, 10, 5941.
- [28] M. Abramchuk, S. Jaszewski, K. R. Metz, G. B. Osterhoudt, Y. Wang, K. S. Burch, F. Tafti, *Adv. Mater.* **2018**, 30, 1801325.
- [29] L. Webster, J.-A. Yan, *Phys. Rev. B* **2018**, 98, 144411.
- [30] Z. Wang, I. Gutierrez-Lezama, N. Ubrig, M. Kroner, M. Gibertini, T. Taniguchi, K. Watanabe, A. Imanoglu, E. Giannini, A. F. Morpurgo, *Nat. Commun.* **2018**, 9, 2516.
- [31] S. Jiang, J. Shan, K. F. Mak, *Nat. Mater.* **2018**, 17, 406.
- [32] B. Huang, G. Clark, D. R. Klein, D. MacNeill, E. Navarro-Moratalla, K. L. Seyler, N. Wilson, M. A. McGuire, D. H. Cobden, D. Xiao, W. Yao, P. Jarillo-Herrero, X. Xu, *Nat. Nanotechnol.* **2018**, 13, 544.
- [33] S. Jiang, L. Li, Z. Wang, K. F. Mak, J. Shan, *Nat. Nanotechnol.* **2018**, 13, 549.
- [34] K. L. Seyler, D. Zhong, D. R. Klein, S. Gao, X. Zhang, B. Huang, E. Navarro-Moratalla, L. Yang, D. H. Cobden, M. A. McGuire, W. Yao, D. Xiao, P. Jarillo-Herrero, X. Xu, *Nat. Phys.* **2017**, 14, 277.
- [35] M. A. McGuire, G. Clark, S. Kc, W. M. Chance, G. E. Jellison, V. R. Cooper, X. Xu, B. C. Sales, *Phys. Rev. Mater.* **2017**, 1, 014001.
- [36] D. R. Klein, D. MacNeill, Q. Song, D. T. Larson, S. Fang, M. Xu, R. A. Ribeiro, P. C. Canfield, E. Kaxiras, R. Comin, P. Jarillo-Herrero, *Nat. Phys.* **2019**, 15, 1255.
- [37] I. Tsubokawa, *J. Phys. Soc. Jpn.* **1960**, 15, 1664.
- [38] Y. Zeng, P. Gu, Z. Zhao, B. Zhang, Z. Lin, Y. Peng, W. Li, W. Zhao, Y. Leng, P. Tan, T. Yang, Z. Zhang, Y. Song, J. Yang, Y. Ye, K. Tian, Y. Hou, *Adv. Mater.* **2022**, 34, 2108847.
- [39] G. Villalpando, A. M. Ferrenti, R. Singha, X. Song, G. Cheng, N. Yao, L. M. Schoop, *ACS Nano* **2022**, 16, 13814.
- [40] N. Zhou, Z. Zhang, F. Wang, J. Li, X. Xu, H. Li, S. Ding, J. Liu, X. Li, Y. Xie, R. Yang, Y. Ma, T. Zhai, *Adv. Sci.* **2022**, 9, 2202177.
- [41] N. Li, L. Zhu, H. Shang, F. Wang, Y. Zhang, Y. Yao, J. Wang, X. Zhan, F. Wang, J. He, Z. Wang, *Nanoscale* **2021**, 13, 6953.
- [42] X. Hu, Z. Jin, Y. Zhong, J. Dai, X. Tao, X. Zhang, J. Han, S. Jiang, L. Zhou, *Chem. Mater.* **2023**, 35, 4220.
- [43] J. Zou, Y. Yang, D. Hu, L. Kang, C. Zhu, D. Tian, X. Lv, G. Kutty, Y. Guo, M. Xu, F. Li, G. Hong, Z. Liu, *SmartMat* **2022**, 3, 482.
- [44] Z. Chen, X. Liu, X. Li, P. Gao, Z. Li, W. Zhu, H. Wang, X. Li, *Nanoscale* **2023**, 15, 8447.
- [45] D. J. O'Hara, T. Zhu, A. H. Trout, A. S. Ahmed, Y. K. Luo, C. H. Lee, M. R. Brenner, S. Rajan, J. A. Gupta, D. W. McComb, R. K. Kawakami, *Nano Lett.* **2018**, 18, 3125.
- [46] L. Kang, C. Ye, X. Zhao, X. Zhou, J. Hu, Q. Li, D. Liu, C. M. Das, J. Yang, D. Hu, J. Chen, X. Cao, Y. Zhang, M. Xu, J. Di, D. Tian, P. Song, G. Kutty, Q. Zeng, Q. Fu, Y. Deng, J. Zhou, A. Ariando, F. Miao, G. Hong, Y. Huang, S. J. Pennycook, K. T. Yong, W. Ji, X. Renshaw Wang, Z. Liu, *Nat. Commun.* **2020**, 11, 3729.
- [47] H. Zhang, Q. Li, M. Hossain, B. Li, K. Chen, Z. Huang, X. Yang, W. Dang, W. Shu, D. Wang, B. Li, W. Xu, Z. Zhang, G. Yu, X. Duan, *Small* **2021**, 17, 2101616.
- [48] Y. Yu, M. Cheng, Z. Tao, W. Han, G. Du, Y. Guo, J. Shi, Y. Chen, *Small* **2024**, 20, 2308357.
- [49] Y. Huan, T. Luo, X. Han, J. Ge, F. Cui, L. Zhu, J. Hu, F. Zheng, X. Zhao, L. Wang, J. Wang, Y. Zhang, *Adv. Mater.* **2023**, 35, 2207276.
- [50] X. Sun, W. Li, X. Wang, Q. Sui, T. Zhang, Z. Wang, L. Liu, D. Li, S. Feng, S. Zhong, H. Wang, V. Bouchiat, M. Nunez Regueiro, N. Rougemaille, J. Coraux, A. Purbawati, A. Hadj-Azzem, Z. Wang, B. Dong, X. Wu, T. Yang, G. Yu, B. Wang, Z. Han, X. Han, Z. Zhang, *Nano Res.* **2020**, 13, 3358.
- [51] H. Wu, W. Zhang, L. Yang, J. Wang, J. Li, L. Li, Y. Gao, L. Zhang, J. Du, H. Shu, H. Chang, *Nat. Commun.* **2021**, 12, 5688.
- [52] W. Yu, J. Li, T. S. Herring, Z. Wang, X. Zhao, X. Chi, W. Fu, I. Abdelwahab, J. Zhou, J. Dan, Z. Chen, Z. Chen, Z. Li, J. Lu, S. J. Pennycook, Y. P. Feng, J. Ding, K. P. Loh, *Adv. Mater.* **2019**, 31, 1903779.
- [53] R. Chua, J. Yang, X. He, X. Yu, W. Yu, F. Bussolotti, P. K. J. Wong, K. P. Loh, M. B. H. Breese, K. E. J. Goh, Y. L. Huang, A. T. S. Wee, *Adv. Mater.* **2020**, 32, 2000693.
- [54] W. Su, A. Kuklin, L. H. Jin, D. Engelhardt, H. Zhang, H. Agren, Y. Zhang, *Adv. Sci.* **2024**, 11, e2402875.
- [55] S. Zhou, R. Wang, J. Han, D. Wang, H. Li, L. Gan, T. Zhai, *Adv. Funct. Mater.* **2019**, 29, 180588.
- [56] F. Cui, X. Zhao, J. Xu, B. Tang, Q. Shang, J. Shi, Y. Huan, J. Liao, Q. Chen, Y. Hou, Q. Zhang, S. J. Pennycook, Y. Zhang, *Adv. Mater.* **2019**, 32, 1905896.
- [57] K. Z. Du, X. Z. Wang, Y. Liu, P. Hu, M. I. Utama, C. K. Gan, Q. Xiong, C. Kloc, *ACS Nano* **2016**, 10, 1738.
- [58] Q. Tan, C. A. Occhipinti, H. Gao, J. Li, H. Kitadai, R. Comin, X. Ling, *Nano Lett.* **2024**, 24, 7166.
- [59] Y. Lee, C. Kim, S. Son, J. Cui, G. Park, K. X. Zhang, S. Oh, H. Cheong, A. Kleibert, J. G. Park, *Nano Lett.* **2024**, 24, 6043.
- [60] K. Hwangbo, Q. Zhang, Q. Jiang, Y. Wang, J. Fonseca, C. Wang, G. M. Diederich, D. R. Gamelin, D. Xiao, J. H. Chu, W. Yao, X. Xu, *Nat. Nanotechnol.* **2021**, 16, 655.
- [61] L. Martin-Perez, S. M. Rivero, M. Vazquez Sulleiro, A. Naranjo, I. J. Gomez, M. L. Ruiz-Gonzalez, A. Castellanos-Gomez, M. Garcia-Hernandez, E. M. Perez, E. Burzuri, *ACS Nano* **2023**, 17, 3007.
- [62] M. J. A. Houmes, S. Mañas-Valero, A. Bermejillo-Seco, E. Coronado, P. G. Steeneken, H. S. J. van der Zant, *Adv. Funct. Mater.* **2023**, 34, 2310206.
- [63] Y. Wang, P. Wang, H. Wang, B. Xu, H. Li, M. Cheng, W. Feng, R. Du, L. Song, X. Wen, X. Li, J. Yang, Y. Cai, J. He, Z. Wang, J. Shi, *Adv. Mater.* **2023**, 35, 2209465.
- [64] Z. Jia, W. Wang, Z. Li, R. Sun, S. Zhou, F. L. Deepak, C. Su, Y. Li, Z. Wang, *ACS Appl. Mater. Interfaces* **2021**, 13, 24051.
- [65] T. Wang, Z. Fan, W. Xue, H. Yang, R. W. Li, X. Xu, *Nano Lett.* **2023**, 23, 10498.
- [66] R. Cheng, L. Yin, Y. Wen, B. Zhai, Y. Guo, Z. Zhang, W. Liao, W. Xiong, H. Wang, S. Yuan, J. Jiang, C. Liu, J. He, *Nat. Commun.* **2022**, 13, 5241.
- [67] P. Wang, J. Ge, J. Luo, H. Wang, L. Song, Z. Li, J. Yang, Y. Wang, R. Du, W. Feng, J. Wang, J. He, J. Shi, *Nano Lett.* **2023**, 23, 1758.
- [68] X. Wang, J. Tang, X. Xia, C. He, J. Zhang, Y. Liu, C. Wan, C. Fang, C. Guo, W. Yang, Y. Guang, X. Zhang, H. Xu, J. Wei, M. Liao, X. Lu, J. Feng, X. Li, Y. Peng, H. Wei, R. Yang, D. Shi, X. Zhang, Z. Han, Z. Zhang, G. Zhang, G. Yu, X. Han, *Sci. Adv.* **2019**, 5, eaaw8904.
- [69] J.-J. Guo, Q.-L. Xia, X.-G. Wang, Y.-Z. Nie, R. Xiong, G.-H. Guo, *J. Magn. Magn. Mater.* **2021**, 527, 167719.
- [70] H. L. Zhuang, P. R. C. Kent, R. G. Hennig, *Phys. Rev. B* **2016**, 93, 134407.
- [71] X. Kong, T. Berlijn, L. Liang, *Adv. Electron. Mater.* **2021**, 7, 2001159.
- [72] B. Das, S. Ghosh, S. Sengupta, P. Auban-Senzier, M. Monteverde, T. K. Dalui, T. Kundu, R. A. Saha, S. Maity, R. Paramanik, A. Ghosh, M. Palit, J. K. Bhattacharjee, R. Mondal, S. Datta, *Small* **2023**, 19, 2302240.
- [73] W. Niu, X. Zhang, W. Wang, J. Sun, Y. Xu, L. He, W. Liu, Y. Pu, *Appl. Phys. Lett.* **2021**, 119, 172402.

- [74] M.-W. Lin, H. L. Zhuang, J. Yan, T. Z. Ward, A. A. Puretzky, C. M. Rouleau, Z. Gai, L. Liang, V. Meunier, B. G. Sumpter, P. Ganesh, P. R. C. Kent, D. B. Geohegan, D. G. Mandrus, K. Xiao, *J. Mater. Chem. C* **2016**, *4*, 315.
- [75] C. Zhang, L. Wang, Y. Gu, X. Zhang, X. Xia, S. Jiang, L. L. Huang, Y. Fu, C. Liu, J. Lin, X. Zou, H. Su, J. W. Mei, J. F. Dai, *Nanoscale* **2022**, *14*, 5851.
- [76] Y. Fang, S. Wu, Z.-Z. Zhu, G.-Y. Guo, *Phys. Rev. B* **2018**, *98*, 125416.
- [77] V. Ostwal, T. Shen, J. Appenzeller, *Adv. Mater.* **2020**, *32*, 1906021.
- [78] W. Zhu, C. Song, L. Han, H. Bai, Q. Wang, S. Yin, L. Huang, T. Chen, F. Pan, *Adv. Funct. Mater.* **2021**, *32*, 2108953.
- [79] I. I. Klimovskikh, M. M. Otrokov, D. Estyunin, S. V. Eremeev, S. O. Filnov, A. Koroleva, E. Shevchenko, V. Voroshnin, A. G. Rybkin, I. P. Rusinov, M. Blanco-Rey, M. Hoffmann, Z. S. Aliev, M. B. Babanly, I. R. Amiraslanov, N. A. Abdullayev, V. N. Zverev, A. Kimura, O. E. Tereshchenko, K. A. Kokh, L. Petaccia, G. Di Santo, A. Ernst, P. M. Echenique, N. T. Mamedov, A. M. Shikin, E. V. Chulkov, *npj Quantum Mater.* **2020**, *5*, 54.
- [80] Y. Li, Y. Wang, Z. Lian, H. Li, Z. Gao, L. Xu, H. Wang, R. Lu, L. Li, Y. Feng, J. Zhu, L. Liu, Y. Wang, B. Fu, S. Yang, L. Yang, Y. Wang, T. Xia, C. Liu, S. Jia, Y. Wu, J. Zhang, Y. Wang, C. Liu, *Nat. Commun.* **2024**, *15*, 3399.
- [81] Y. Wen, Z. Liu, Y. Zhang, C. Xia, B. Zhai, X. Zhang, G. Zhai, C. Shen, P. He, R. Cheng, L. Yin, Y. Yao, M. G. Sendeku, Z. Wang, X. Ye, C. Liu, C. Jiang, C. Shan, Y. Long, J. He, *Nano Lett.* **2020**, *20*, 3130.
- [82] M. Hossain, B. Qin, B. Li, X. Duan, *Nano Today* **2022**, *42*, 101338.
- [83] Z. Fei, B. Huang, P. Malinowski, W. Wang, T. Song, J. Sanchez, W. Yao, D. Xiao, X. Zhu, A. F. May, W. Wu, D. H. Cobden, J.-H. Chu, X. Xu, *Nat. Mater.* **2018**, *17*, 778.
- [84] L. D. Casto, A. J. Clune, M. O. Yokosuk, J. L. Musfeldt, T. J. Williams, H. L. Zhuang, M. W. Lin, K. Xiao, R. G. Hennig, B. C. Sales, J. Q. Yan, D. Mandrus, *APL Mater.* **2015**, *3*, 041515.
- [85] T. Song, X. Cai, M. W.-Y. Tu, X. Zhang, B. Huang, N. P. Wilson, K. L. Seyler, L. Zhu, T. Taniguchi, K. Watanabe, M. A. McGuire, D. H. Cobden, D. Xiao, W. Yao, X. Xu, *Science* **2018**, *360*, 1214.
- [86] K. Lasek, P. M. Coelho, K. Zberecki, Y. Xin, S. K. Kolekar, J. Li, M. Batzill, *ACS Nano* **2020**, *14*, 8473.
- [87] Q.-Q. Yuan, Z. Guo, Z.-Q. Shi, H. Zhao, Z.-Y. Jia, Q. Wang, J. Sun, D. Wu, S.-C. Li, *Chin. Phys. Lett.* **2020**, *37*, 077502.
- [88] L. Sun, G. Yuan, L. Gao, J. Yang, M. Chhowalla, M. H. Gharahcheshmeh, K. K. Gleason, Y. S. Choi, B. H. Hong, Z. Liu, *Nat. Rev. Methods Primers* **2021**, *1*, 5.
- [89] G. Xue, X. Sui, P. Yin, Z. Zhou, X. Li, Y. Cheng, Q. Guo, S. Zhang, Y. Wen, Y. Zuo, C. Zhao, M. Wu, P. Gao, Q. Li, J. He, E. Wang, G. Zhang, C. Liu, K. Liu, *Sci. Bull.* **2023**, *68*, 1514.
- [90] N. Briggs, S. Subramanian, Z. Lin, X. Li, X. Zhang, K. Zhang, K. Xiao, D. Geohegan, R. Wallace, L.-Q. Chen, M. Terrones, A. Ebrahimi, S. Das, J. Redwing, C. Hinkle, K. Momeni, A. van Duin, V. Crespi, S. Kar, J. A. Robinson, *2D Mater.* **2019**, *6*, 022001.
- [91] L. Li, Y. Yu, G. J. Ye, Q. Ge, X. Ou, H. Wu, D. Feng, X. H. Chen, Y. Zhang, *Nat. Nanotechnol.* **2014**, *9*, 372.
- [92] M. Lanza, Q. Smets, C. Huyghebaert, L. J. Li, *Nat. Commun.* **2020**, *11*, 5689.
- [93] Y. Huang, Y.-H. Pan, R. Yang, L.-H. Bao, L. Meng, H.-L. Luo, Y.-Q. Cai, G.-D. Liu, W.-J. Zhao, Z. Zhou, L.-M. Wu, Z.-L. Zhu, M. Huang, L.-W. Liu, L. Liu, P. Cheng, K.-H. Wu, S.-B. Tian, C.-Z. Gu, Y.-G. Shi, Y.-F. Guo, Z. G. Cheng, J.-P. Hu, L. Zhao, G.-H. Yang, E. Sutter, P. Sutter, Y.-L. Wang, W. Ji, X.-J. Zhou, H.-J. Gao, *Nat. Commun.* **2020**, *11*, 2453.
- [94] J.-Y. Moon, M. Kim, S.-I. Kim, S. Xu, J.-H. Choi, D. Whang, K. Watanab, T. Taniguchi, D. S. Park, J. Seo, S. H. Cho, S.-K. Son, J.-H. Lee, *Sci. Adv.* **2020**, *6*, eabc6601.
- [95] J. Shiogai, Y. Ito, T. Mitsuhashi, T. Nojima, A. Tsukazaki, *Nat. Phys.* **2015**, *12*, 42.
- [96] J. Feng, X. Sun, C. Wu, L. Peng, C. Lin, S. Hu, J. Yang, Y. Xie, *J. Am. Chem. Soc.* **2011**, *133*, 17832.
- [97] Y. Guo, H. Deng, X. Sun, X. Li, J. Zhao, J. Wu, W. Chu, S. Zhang, H. Pan, X. Zheng, X. Wu, C. Jin, C. Wu, Y. Xie, *Adv. Mater.* **2017**, *29*, 1700715.
- [98] K. K. S. Lau, J. Bico, K. B. K. Teo, M. Chhowalla, G. A. J. Amarasingha, W. I. Milne, G. H. McKinley, K. K. Gleason, *Nano Lett.* **2003**, *3*, 1701.
- [99] W. S. O'Shaughnessy, S. K. Murthy, D. J. Edell, K. K. Gleason, *Biomacromolecules* **2007**, *8*, 2564.
- [100] Y. Wang, X. Zhan, F. Wang, Q. Wang, M. Safdar, J. He, *J. Mater. Chem. A* **2014**, *2*, 18413.
- [101] X. Li, W. Cai, J. An, S. Kim, J. Nah, D. Yang, R. Piner, A. Velamakanni, I. Jung, E. Tutuc, S. K. Banerjee, L. Colombo, R. S. Ruoff, *Science* **2009**, *324*, 1312.
- [102] M. C. Barr, J. A. Rowehl, R. R. Lunt, J. Xu, A. Wang, C. M. Boyce, S. G. Im, V. Bulović, K. K. Gleason, *Adv. Mater.* **2011**, *23*, 3500.
- [103] S. Ullah, X. Q. Yang, H. Q. Ta, M. Hasan, A. Bachmatiuk, K. Tokarska, B. Trzebicka, L. Fu, M. H. Rummeli, *Nano Res.* **2021**, *14*, 3756.
- [104] S. Roy, X. Zhang, A. B. Puthirath, A. Meiyazhagan, S. Bhattacharyya, M. M. Rahman, G. Babu, S. Susarla, S. K. Saju, M. K. Tran, L. M. Sassi, M. Saadi, J. W. Lai, O. Sahin, S. M. Sajadi, B. Dharmarajan, D. Salpekar, N. Chakingal, A. Baburaj, X. T. Shuai, A. Adumbumkulath, K. A. Miller, J. M. Gayle, A. Ajnsztajn, T. Prasankumar, V. V. J. Harikrishnan, V. Ojha, H. Kannan, A. Z. Khater, Z. W. Zhu, et al., *Adv. Mater.* **2021**, *33*, 2101589.
- [105] Z. M. Ye, C. Tan, X. L. Huang, Y. Ouyang, L. Yang, Z. G. Wang, M. D. Dong, *Nano-Micro Lett.* **2023**, *15*, 38.
- [106] J. Li, B. Zhao, P. Chen, R. Wu, B. Li, Q. Xia, G. Guo, J. Luo, K. Zang, Z. Zhang, H. Ma, G. Sun, X. Duan, X. Duan, *Adv. Mater.* **2018**, *30*, 1801043.
- [107] C. Chen, X. Chen, C. Wu, X. Wang, Y. Ping, X. Wei, X. Zhou, J. Lu, L. Zhu, J. Zhou, T. Zhai, J. Han, H. Xu, *Adv. Mater.* **2022**, *34*, 2107512.
- [108] B. Li, Z. Wan, C. Wang, P. Chen, B. Huang, X. Cheng, Q. Qian, J. Li, Z. Zhang, G. Sun, B. Zhao, H. Ma, R. Wu, Z. Wei, Y. Liu, L. Liao, Y. Ye, Y. Huang, X. Xu, X. Duan, W. Ji, X. Duan, *Nat. Mater.* **2021**, *20*, 818.
- [109] Y. Zhang, J. Chu, L. Yin, T. A. Shifa, Z. Cheng, R. Cheng, F. Wang, Y. Wen, X. Zhan, Z. Wang, J. He, *Adv. Mater.* **2019**, *31*, 1900056.
- [110] J. Chu, Y. Zhang, Y. Wen, R. Qiao, C. Wu, P. He, L. Yin, R. Cheng, F. Wang, Z. Wang, J. Xiong, Y. Li, J. He, *Nano Lett.* **2019**, *19*, 2154.
- [111] J. Jiang, R. Cheng, W. Feng, L. Yin, Y. Wen, Y. Wang, Y. Cai, Y. Liu, H. Wang, B. Zhai, C. Liu, J. He, Z. Wang, *Adv. Mater.* **2023**, *35*, 2211701.
- [112] W. Li, X. Qiu, B. Lv, B. Zhang, J. Tang, J. Xu, K. Tian, Z. Zhao, Y. Zeng, X. Huang, H. Du, Y. Hou, *Matter* **2022**, *5*, 291.
- [113] M. Bahri, S. H. Gebre, M. A. Elaguech, F. T. Dajan, M. G. Sendeku, C. Tlili, D. Wang, *Coord. Chem. Rev.* **2023**, *475*, 214910.
- [114] R. W. Johnson, A. Hultqvist, S. F. Bent, *Mater. Today* **2014**, *17*, 236.
- [115] P. Wang, Y. Wen, X. Zhao, B. Zhai, R. Du, M. Cheng, Z. Liu, J. He, J. Shi, *ACS Nano* **2022**, *16*, 8301.
- [116] S. Luo, X. Zhu, H. Liu, S. Song, Y. Chen, C. Liu, W. Zhou, C. Tang, G. Shao, Y. Jin, J. Guan, V. C. Tung, H. Li, X. Chen, F. Ouyang, S. Liu, *Chem. Mater.* **2022**, *34*, 2342.
- [117] M. Zhu, Q. Li, K. Guo, B. Chen, K. He, C. Yi, P. Lu, X. Li, J. Lu, J. Li, R. Wu, X. Liu, Y. Liu, L. Liao, B. Li, X. Duan, *Nano Lett.* **2024**, *24*, 7483.
- [118] Q. Shi, K. Tokarska, H. Q. Ta, X. Yang, Y. Liu, S. Ullah, L. Liu, B. Trzebicka, A. Bachmatiuk, J. Sun, L. Fu, Z. Liu, M. H. Rummeli, *Adv. Mater. Interfaces* **2020**, *7*, 1902024.
- [119] L. Song, Y. Zhao, R. Du, H. Li, X. Li, W. Feng, J. Yang, X. Wen, L. Huang, Y. Peng, H. Sun, Y. Jiang, J. He, J. Shi, *Nano Lett.* **2024**, *24*, 2408.
- [120] Z. Jin, Z. Ji, Y. Zhong, Y. Jin, X. Hu, X. Zhang, L. Zhu, X. Huang, T. Li, X. Cai, L. Zhou, *ACS Nano* **2022**, *16*, 7572.

- [121] H. Zhang, J. Tang, B. Li, B. Li, Z. Zhang, K. He, S. Shi, X. Shen, J. Liu, Z. Huang, D. Wang, W. Deng, M. Liu, X. Zhou, X. Duan, *Nano Today* **2023**, *49*, 101794.
- [122] H. Wang, Y. Wen, X. Zhao, R. Cheng, L. Yin, B. Zhai, J. Jiang, Z. Li, C. Liu, F. Wu, J. He, *Adv. Mater.* **2023**, *35*, 2211388.
- [123] H. Jiang, P. Zhang, X. Wang, Y. Gong, *Nano Res.* **2020**, *14*, 1789.
- [124] J. You, J. Pan, S. L. Shang, X. Xu, Z. Liu, J. Li, H. Liu, T. Kang, M. Xu, S. Li, D. Kong, W. Wang, Z. Gao, X. Zhou, T. Zhai, Z. K. Liu, J. K. Kim, Z. Luo, *Nano Lett.* **2022**, *22*, 10167.
- [125] Q. Jiang, H. Yang, W. Xue, R. Yang, J. Shen, X. Zhang, R. W. Li, X. Xu, *Nano Lett.* **2024**, *24*, 1246.
- [126] C. Gong, X. Zhang, *Science* **2019**, *363*, 706.
- [127] L. Meng, Z. Zhou, M. Xu, S. Yang, K. Si, L. Liu, X. Wang, H. Jiang, B. Li, P. Qin, P. Zhang, J. Wang, Z. Liu, P. Tang, Y. Ye, W. Zhou, L. Bao, H. J. Gao, Y. Gong, *Nat. Commun.* **2021**, *12*, 809.
- [128] S. A. Wolf, D. D. Awschalom, R. A. Buhrman, J. M. Daughton, S. v. Molná'r, M. L. Roukes, A. Y. Chtchelkanova, D. M. Treger, *Science* **2001**, *294*, 1488.
- [129] I. Z'utic', J. Fabian, S. D. Sarma, *Rev. Mod. Phys.* **2004**, *76*, 323.
- [130] S. Manzeli, D. Ovchinnikov, D. Pasquier, O. V. Yazyev, A. Kis, *Nat. Rev. Mater.* **2017**, *2*, 17033.
- [131] M. Julliere, *Phys. Lett. A* **1975**, *54*, 225.
- [132] Y. Tserkovnyak, A. Brataas, G. E. W. Bauer, B. I. Halperin, *Rev. Mod. Phys.* **2005**, *77*, 1375.
- [133] J. S. Moodera, L. R. Kinder, T. M. Wong, R. Meservey, *Phys. Rev. Lett.* **1995**, *74*, 3273.
- [134] S. Bhatti, R. Sbiaa, A. Hirohata, H. Ohno, S. Fukami, S. N. Piramanayagam, *Mater. Today* **2017**, *20*, 530.
- [135] A. K. Geim, I. V. Grigorieva, *Nature* **2013**, *499*, 419.
- [136] G. Zhang, F. Guo, H. Wu, X. Wen, L. Yang, W. Jin, W. Zhang, H. Chang, *Nat. Commun.* **2022**, *13*, 5067.
- [137] W. Jin, G. Zhang, H. Wu, L. Yang, W. Zhang, H. Chang, *ACS Appl. Mater. Interfaces* **2023**, *15*, 36519.
- [138] M. N. Baibich, J. M. Broto, A. Fert, F. N. Van Dau, F. Petroff, P. Etienne, G. Creuzet, A. Friederich, J. Chazelas, *Phys. Rev. Lett.* **1988**, *61*, 2472.
- [139] B. Diény, V. S. Speriosu, S. S. P. Parkin, B. A. Gurney, D. R. Wilhoit, D. Mauri, *Phys. Rev. B* **1991**, *43*, 1297.
- [140] A. Hirohata, K. Yamada, Y. Nakatani, I.-L. Prejbeanu, B. Diény, P. Pirro, B. Hillebrands, *J. Magn. Magn. Mater.* **2020**, *509*, 166711.
- [141] K. Hirose, D. Kobayashi, T. Ito, T. Endoh, *Jpn. J. Appl. Phys.* **2017**, *56*, 0802A5.
- [142] D. Cho, K. M. Bastiaans, D. Chatzopoulos, G. D. Gu, M. P. Allan, *Nature* **2019**, *571*, 541.
- [143] Z. gao, J. Chen, Z. Zhang, Z. Liu, Y. Zhang, L. Xu, J. Wu, F. Luo, *Adv. Electron. Mater.* **2022**, *9*, 2200823.
- [144] B. Zhao, B. Karpiak, D. Khokhriakov, A. Johansson, A. M. Hoque, X. Xu, Y. Jiang, I. Mertig, S. P. Dash, *Adv. Mater.* **2020**, *32*, 2000818.
- [145] B. Zhao, R. Ngalo, S. Ghosh, S. Ershadrad, R. Gupta, K. Ali, A. M. Hoque, B. Karpiak, D. Khokhriakov, C. Polley, B. Thiagarajan, A. Kalaboukhov, P. Svedlindh, B. Sanyal, S. P. Dash, *Adv. Mater.* **2023**, *35*, 2209113.
- [146] M. Alghamdi, M. Lohmann, J. Li, P. R. Jothi, Q. Shao, M. Aldosary, T. Su, B. P. T. Fokwa, J. Shi, *Nano Lett.* **2019**, *19*, 4400.
- [147] S. Datta, B. Das, *Appl. Phys. Lett.* **1989**, *56*, 3.
- [148] S. Sugahara, M. Tanaka, *Appl. Phys. Lett.* **2004**, *84*, 2307.
- [149] S. Manipatruni, D. E. Nikonorov, C.-C. Lin, T. A. Gosavi, H. Liu, B. Prasad, Y.-L. Huang, E. Bonturim, R. Ramesh, I. A. Young, *Nature* **2019**, *565*, 35.
- [150] A. Dankert, S. P. Dash, *Nat. Commun.* **2017**, *8*, 16093.
- [151] T. S. Ghias, J. Inglá-Aynés, A. A. Kaverzin, B. J. v. Wees, *Nano Lett.* **2017**, *17*, 7528.
- [152] S.-J. Gong, C. Gong, Y.-Y. Sun, W.-Y. Tong, C.-G. Duan, J.-H. Chu, X. Zhang, *Proc. Natl. Acad. Sci. USA* **2018**, *115*, 8511.
- [153] M. Bonilla, S. Kolekar, Y. Ma, H. C. Diaz, V. Kalappattil, R. Das, T. Eggers, H. R. Gutierrez, M.-H. Phan, M. Batzill, *Nat. Nanotechnol.* **2018**, *13*, 289.
- [154] S. Jiang, L. Li, Z. Wang, J. Shan, K. F. Mak, *Nat. Electron.* **2019**, *2*, 159.
- [155] C. Psaroudaki, C. Panagopoulos, *Phys. Rev. Lett.* **2021**, *127*, 067201.
- [156] W. Zhu, J. Sun, Y. Wang, Y. Li, H. Bai, Q. Wang, L. Han, Q. Zhang, H. Wu, C. Song, F. Pan, *Adv. Mater.* **2024**, *36*, e2403624.
- [157] G. S. Joyce, *Phys. Rev.* **1967**, *155*, 478.
- [158] B. A. Cipra, *Am. Math. Mon.* **2018**, *94*, 937.
- [159] F. Kos, D. Poland, D. Simmons-Duffin, A. Vichi, *J. High Energy Phys.* **2016**, *2016*, 36.
- [160] X. Wang, *Phys. Rev. A* **2001**, *64*, 012313.
- [161] N. Miao, Z. Sun, *WIREs Comput. Mol. Sci.* **2021**, *12*, e1545.
- [162] S. Lu, Q. Zhou, Y. Guo, Y. Zhang, Y. Wu, J. Wang, *Adv. Mater.* **2020**, *32*, e2002658.
- [163] L. Zhang, J. Zhou, H. Li, L. Shen, Y. P. Feng, *Appl. Phys. Rev.* **2021**, *8*, 021308.
- [164] C. Dai, P. He, L. Luo, P. Zhan, B. Guan, J. Zheng, *Sci. China Mater.* **2023**, *66*, 859.
- [165] H. Kurebayashi, J. H. Garcia, S. Khan, J. Sinova, S. Roche, *Nat. Rev. Phys.* **2022**, *4*, 150.
- [166] L. Lv, L. Hu, W. Dong, J. Duan, P. Wang, P. Li, F. Qu, L. Lu, Z. Ye, J. Zhao, J. Li, F. Deng, G. Liu, J. Zhou, Y. Gao, *Adv. Funct. Mater.* **2024**, *34*, 2401748.



Shuyang Yuan is currently an undergraduate student under the supervision of Prof. Jun He at the School of Physics and Technology, Wuhan University. His main research interest is focused on developing low-dimensional materials for high-performance electronic, ferroelectric and magnetic devices.



Yanchang Zhou is currently a Ph.D. candidate under the supervision of Prof. Jun He at the School of Physics and Technology, Wuhan University. His main research interest is focused on developing low-dimensional materials for high-performance electronic, ferroelectric and magnetic devices.



Ruiqing Cheng received his bachelor's degree in physics from Shandong University, master's degree in Nanoscience and Technology from University of Copenhagen, and Ph.D. degree in Condensed Matter Physics from National Center for Nanoscience and Technology. He is currently an associate professor at the School of Physics and Technology, Wuhan University. His research mainly focuses on low-dimensional semiconductors and their device applications.



Jun He received his Ph.D. degree in Semiconductor Physics from the Institute of Semiconductors, Chinese Academy of Sciences in 2003. He is currently a full professor at the School of Physics and Technology, Wuhan University. His main research interest is the synthesis, characterization, and devices of low-dimensional semiconductor materials.